



HAL
open science

An asymptotic preserving scheme on staggered grids for the barotropic Euler system in low Mach regimes

Thierry Goudon, Julie Llobell, Sebastian Minjeaud

► To cite this version:

Thierry Goudon, Julie Llobell, Sebastian Minjeaud. An asymptotic preserving scheme on staggered grids for the barotropic Euler system in low Mach regimes. *Numerical Methods for Partial Differential Equations*, 2020, 36 (5), pp.1098-1128. hal-02418641

HAL Id: hal-02418641

<https://inria.hal.science/hal-02418641>

Submitted on 10 Dec 2020

HAL is a multi-disciplinary open access archive for the deposit and dissemination of scientific research documents, whether they are published or not. The documents may come from teaching and research institutions in France or abroad, or from public or private research centers.

L'archive ouverte pluridisciplinaire **HAL**, est destinée au dépôt et à la diffusion de documents scientifiques de niveau recherche, publiés ou non, émanant des établissements d'enseignement et de recherche français ou étrangers, des laboratoires publics ou privés.

An asymptotic preserving scheme on staggered grids for the barotropic Euler system in low Mach regimes

Thierry Goudon, Julie Llobell, Sebastian Minjeaud

Université Côte d’Azur, Inria, CNRS, LJAD

Abstract. We present a new scheme for the simulation of the barotropic Euler equation in low Mach regimes. The method uses two main ingredients. First, the system is treated with a suitable time splitting strategy, directly inspired from [J. Haack, S. Jin, J.-G. Liu, *Comm. Comput. Phys.*, 12 (2012) 955–980], that separates low and fast waves. Second, we adapt a numerical scheme where the discrete densities and velocities are stored on staggered grids, in the spirit of MAC methods, and with numerical fluxes derived from the kinetic approach. We bring out the main properties of the scheme in terms of consistency, stability, and asymptotic behaviour, and we present a series of numerical experiments to validate the method.

MSC. 65M08, 76M12, 76NXX, 35Q31.

Contents

1	Introduction	1
1.1	Euler equations and low Mach regimes	1
1.2	Low Mach regimes	2
1.3	Numerical issues of the low Mach regimes	3
1.4	A new numerical strategy	4
2	Numerical resolution	4
2.1	Splitting of the compressible Euler system	4
2.2	Time discretization and stability	6
2.3	Space discretization	7
2.4	Low Mach regimes and AP-scheme	11
3	Numerical simulations	17
3.1	Simulation of 1D Riemann problems in low Mach regime	17
3.2	Low Mach regime simulations in 2D	19
3.2.1	Test 1: traveling vortex	19
3.2.2	Test 2: cylindrical explosion problem	24
3.2.3	Test 3	27
3.3	Incompressible Euler simulations using the limit scheme	28
3.3.1	Test A: analytical solution	28
3.3.2	Test B: double shear layer	29

1 Introduction

1.1 Euler equations and low Mach regimes

This work is concerned with the numerical resolution of the barotropic Euler system, which describes the evolution of a compressible fluid, in low Mach regimes. The unknowns ρ and \mathbf{u} stand respectively for the local density and velocity of the fluid. They both depend on the time and space variables, $t \geq 0$ and $x \in \Omega \subset \mathbb{R}^N$, where Ω is a bounded domain. Working with dimensionless quantities, the evolution of the fluid is governed by the PDE system

$$\begin{cases} \partial_t \rho + \nabla \cdot (\rho \mathbf{u}) = 0, \\ \partial_t (\rho \mathbf{u}) + \nabla \cdot (\rho \mathbf{u} \otimes \mathbf{u}) + \frac{1}{\epsilon^2} \nabla p(\rho) = 0. \end{cases} \quad (1)$$

The system has obviously to be completed with initial and boundary conditions (periodic or vanishing flux for instance). Here and below, we suppose that the pressure law $\rho \mapsto p(\rho)$ is the classical power-law $p(\rho) = \rho^\gamma$ with $\gamma > 1$. In (1), ϵ stands for the Mach number, that is the ratio of the typical velocity of the fluid to the typical sound speed ($\epsilon^2 = \frac{|\mathbf{u}_{\text{ref}}|^2}{c_{\text{ref}}^2} = \frac{\rho_{\text{ref}} |\mathbf{u}_{\text{ref}}|^2}{\gamma p_{\text{ref}}}$). We are interested in the numerical approximations of the solution of system (1) for $0 < \epsilon \leq 1$ varying from very small values to unity.

1.2 Low Mach regimes

In order to understand the behaviour for small ϵ 's, let us expand the solution as a power series $Q = Q^{(0)} + \epsilon Q^{(1)} + \epsilon^2 Q^{(2)} + \dots$, with $Q = (\rho, p, \mathbf{u})$, and identify the terms that arise with the same order of magnitude with respect to ϵ in (1). At the leading order $\mathcal{O}(1/\epsilon^2)$ in the momentum equation, we obtain $\nabla p^{(0)} = 0$ from what we deduce $p^{(0)}(x, t) = p^{(0)}(t)$ and consequently $\rho^{(0)}(x, t) = \rho^{(0)}(t)$. Similarly, at order $\mathcal{O}(1/\epsilon)$ we get $\nabla p^{(1)} = 0$, thus $\rho^{(1)}(x, t) = \rho^{(1)}(t)$ depends only on the time variable too. Given this information, system (1) at order $\mathcal{O}(1)$ becomes

$$\begin{cases} \partial_t \rho^{(0)} + \rho^{(0)} \nabla \cdot \mathbf{u}^{(0)} = 0, \\ \partial_t (\rho^{(0)} \mathbf{u}^{(0)}) + \rho^{(0)} \nabla \cdot (\mathbf{u}^{(0)} \otimes \mathbf{u}^{(0)}) + \nabla p^{(2)} = 0. \end{cases} \quad (2)$$

Integrating the mass equation in (2) over the domain Ω , yields

$$\int_{\Omega} \left(\partial_t \rho^{(0)} + \rho^{(0)} \nabla \cdot \mathbf{u}^{(0)} \right) dx = |\Omega| \partial_t \rho^{(0)} + \rho^{(0)} \int_{\Omega} \nabla \cdot \mathbf{u}^{(0)} dx = 0.$$

Applying the Green theorem leads to

$$\partial_t \rho^{(0)} = -\frac{1}{|\Omega|} \rho^{(0)} \int_{\partial\Omega} \mathbf{u}^{(0)} \cdot \mathbf{n} d\sigma(x)$$

where \mathbf{n} is the outward-pointing normal vector on $\partial\Omega$ and $d\sigma(x)$ is the Lebesgue measure. Let us restrict to the case of zero-flux boundary conditions, $\mathbf{u} \cdot \mathbf{n}|_{\partial\Omega} = 0$, or the case of periodic boundary conditions, so that in both cases we have $\int_{\partial\Omega} \mathbf{u}^{(0)} \cdot \mathbf{n} d\sigma(x) = 0$. It follows that $\partial_t \rho^{(0)} = 0$. Going back to the mass conservation equation in (2) we arrive at

$$\nabla \cdot \mathbf{u}^{(0)}(x, t) = 0 \quad \text{and} \quad \rho^{(0)}(x, t) = \rho^{(0)} \quad \text{on} \quad \Omega \times [0, \infty).$$

The momentum equation in (2) can now be cast as

$$\partial_t \mathbf{u}^{(0)} + \nabla \cdot (\mathbf{u}^{(0)} \otimes \mathbf{u}^{(0)}) + \frac{1}{\rho^{(0)}} \nabla p^{(2)} = 0.$$

In this relation the pressure term $p^{(2)}$ can be seen as the Lagrange multiplier associated to the incompressibility constraint $\nabla \cdot \mathbf{u}^{(0)} = 0$. Applying the divergence operator we are led to

$$\Delta p^{(2)} = -\rho^{(0)} \nabla \cdot (\nabla \cdot (\mathbf{u}^{(0)} \otimes \mathbf{u}^{(0)})).$$

Finally, the mass equation in (1) at order $\mathcal{O}(\epsilon)$ reads

$$\partial_t \rho^{(1)} + \rho^{(0)} \nabla \cdot \mathbf{u}^{(1)} = 0.$$

With a similar reasoning, we deduce that $\rho^{(1)}(x, t) = \rho^{(1)}$ is constant in time and space and that $\nabla \cdot \mathbf{u}^{(1)} = 0$.

Definition 1.1. The initial data $(\rho, \mathbf{u})(x, t = 0)$ for (1) is said to be well-prepared when

$$\begin{aligned} \rho(x, t = 0) &= \rho^{(0)} + \epsilon \rho^{(1)} + \mathcal{O}(\epsilon^2)(x) \text{ with } \rho^{(0)}, \rho^{(1)} \text{ real constants,} \\ \mathbf{u}(x, t = 0) &= \mathbf{u}^{(0)}(x, t = 0) + \mathcal{O}(\epsilon)(x) \text{ with } \nabla \cdot \mathbf{u}^{(0)}(x, t = 0) = 0. \end{aligned}$$

Therefore, as ϵ goes to 0, we expect that solutions (ρ, \mathbf{u}) of (1) behave like

$$\begin{aligned} \rho(x, t) &= \rho^{(0)} + \epsilon \rho^{(1)} + \mathcal{O}(\epsilon^2)(x, t), \\ \mathbf{u}(x, t) &= \mathbf{u}^{(0)}(x, t) + \mathcal{O}(\epsilon)(x, t) \end{aligned}$$

with $\mathbf{u}^{(0)}$ solution of the Incompressible Euler system

$$\partial_t \mathbf{u}^{(0)} + \nabla \cdot (\mathbf{u}^{(0)} \otimes \mathbf{u}^{(0)}) + \frac{1}{\rho^{(0)}} \nabla p^{(2)} = 0, \quad \nabla \cdot \mathbf{u}^{(0)} = 0. \quad (3)$$

Further details on the low Mach asymptotics can be found in A. Majda's book [32]. Rigorous justification dates back to [27, 28]. When the initial data are not well-prepared, initial layer might occur [37]. We refer the interested reader to [1] for an up-to-date review detailing further results and indicating further relevant references on the analysis of the low Mach regimes.

1.3 Numerical issues of the low Mach regimes

There are several numerical issues that make the simulation of (1) challenging as ϵ becomes small:

- The stiffness of the pressure term induces severe stability conditions for standard time-explicit schemes. Indeed, the characteristic speeds of the system behave like $|\mathbf{u}| \pm \frac{1}{\epsilon} \sqrt{p'(\rho)}$ and thus become very large as $\epsilon \rightarrow 0$. It imposes to constrain the time step δt to be proportional to $\epsilon \delta x$ with δx the mesh size, which leads to non affordable computational costs.
- Moreover, the usual conservative finite-volume type schemes are also subject to a dramatic loss of accuracy when ϵ becomes small, so that it can be very difficult to capture the correct solution. This phenomena has been brought out in the seminal papers [17, 19] which explain how Godunov type schemes create spurious pressure waves that prevent the discrete solutions to be close to a discrete incompressible flow. This has been further analyzed in [2, 9, 10, 11, 12]. It turns out that the loss of accuracy in fact highly depends on the geometry of the mesh [18]. In particular UpWind schemes on Cartesian meshes (that we shall consider here) are inaccurate at low Mach numbers. These analysis have led to design suitable preconditioning techniques [17, 19, 36].

We are thus faced with the difficulty of designing numerical methods that preserve the asymptotic limit, without inducing too high computational costs. A possible avenue to cope with these difficulties is to try to develop “Asymptotic Preserving” methods, a term coined by S. Jin [24, 25].

Definition 1.2. *Asymptotic Preserving (AP) Method.*

A method is said to be AP when it preserves at the discrete level the asymptotic passage from a model to another. To be more specific, if the space and time steps δx and δt are kept fixed, the method automatically transforms to a stable discretization of the limit model when the small scale parameter tends to zero.

Such methods are intended to be robust in the sense that the asymptotic regimes can be captured without resolving the small time and spatial scales. The efficiency of an AP scheme relies on careful time and space discretizations. Since we expect to make use of time steps much larger than the one imposed by the standard CFL conditions, it is clear that a part of the system should be treated implicitly to overcome the stiffness. However, the numerical cost of the implicit solver should remain as reduced as possible. We can mention [8, 14, 20, 29, 34] for attempts in that direction.

1.4 A new numerical strategy

In this work, we wish to develop an AP procedure by following the ideas introduced by J. Haack, S. Jin and J.-G. Liu in [20]. The stiff Euler system is split into two parts: a nonlinear and hyperbolic system of conservation laws that involves only waves propagating with $\mathcal{O}(1)$ speeds, and a linear system that contains the fast acoustic dynamics. The former equations are treated explicitly, the latter are treated implicitly. Next, in this framework, we propose a space discretization that relies on strategies introduced in [3] and that presents the following originalities:

- we work on staggered grids, with densities (and thus pressures) and velocities stored on dual locations. This is not usual for hyperbolic conservation laws. However, this approach is well suited to avoid spurious oscillations in regimes close to incompressible: on Cartesian grids, we can expect to recover a final scheme based on the principles of MAC schemes [21]. This approach is also developed, possibly with a different definition of numerical fluxes though, in e. g. [4, 16, 22, 23, 39].
- the numerical fluxes are defined with an inspiration from kinetic schemes, see [7, 13] and the references therein. It provides simple formulae, which permit us to justify the positivity of the density and the entropy-stability [3]. We also refer the reader to [31] for further developments of the method, in particular its extension to second order (using MUSCL-like techniques and a RK2 scheme) and to the full Euler system.

Remark 1.3. We point out that the inspiration from the kinetic viewpoint has been recently used to develop new methods for solving the Incompressible Navier-Stokes system [5], with interesting theoretical properties, in particular with respect to energy/entropy dissipation. Note however that, despite the derivation of this method relies on asymptotic analysis and the introduction of vanishing Mach numbers, it is *not* designed for performing well in low Mach regimes.

The paper is organized as follows. In Section 2.1 we describe the time splitting strategy of [20]. In Section 2.2 and 2.3 we detail the construction of our scheme. Section 2.4 investigates the properties of the method: we show how the scheme becomes a (simple) incompressible solver as $\epsilon \rightarrow 0$ and we check that well-prepared data do not produce spurious oscillations, according to the analysis of [9, 10, 12]. Finally, we discuss a set of numerical experiments in Section 3.

2 Numerical resolution

2.1 Splitting of the compressible Euler system

The compressible system (1) is split with two scales: the fast acoustics wave scale and the slow convection scale that contains the underlying incompressible dynamics. Following [20], we rewrite the system in the following way

$$\begin{cases} \partial_t \rho + \alpha \nabla \cdot (\rho \mathbf{u}) + (1 - \alpha) \nabla \cdot (\rho \mathbf{u}) = 0, \\ \partial_t (\rho \mathbf{u}) + \nabla \cdot (\rho \mathbf{u} \otimes \mathbf{u}) + \nabla \cdot \left(\frac{p(\rho) - a(t)\rho}{\epsilon^2} \right) + \frac{a(t)}{\epsilon^2} \nabla \rho = 0. \end{cases} \quad (4)$$

The parameter $0 \leq \alpha < 1$ is used in order to keep some momentum in the system for the fast dynamics, see (FD) below, which is necessary to enforce incompressibility. The splitting of the stiff pressure term also involves a new parameter $a(t) > 0$.

For the numerical resolution of (4) we adopt the following time-splitting strategy that makes the two distinct scales appear. We start with the Slow Dynamics system, the hyperbolic system of conservation laws that reads

$$\begin{cases} \partial_t \rho + \alpha \nabla \cdot (\rho \mathbf{u}) = 0, \\ \partial_t (\rho \mathbf{u}) + \nabla \cdot (\rho \mathbf{u} \otimes \mathbf{u}) + \nabla \cdot \left(\frac{p(\rho) - a(t)\rho}{\epsilon^2} \right) = 0. \end{cases} \quad (\text{SD})$$

Then, we consider the following Fast Dynamics system

$$\begin{cases} \partial_t \rho + (1 - \alpha) \nabla \cdot (\rho \mathbf{u}) = 0, \\ \partial_t (\rho \mathbf{u}) + \frac{a(t)}{\epsilon^2} \nabla \rho = 0. \end{cases} \quad (\text{FD})$$

Let us focus on the two-dimensional framework. Denoting u and v the components of the velocity field $\mathbf{u} = (u, v)$, the wave speeds of the (SD) in the horizontal (resp. vertical) direction are given by u (resp. v) and $\tilde{\lambda}_{\pm}(\rho, u)$ (resp. $\tilde{\lambda}_{\pm}(\rho, v)$) where

$$\tilde{\lambda}_{\pm}(\rho, \nu) = \nu \pm \tilde{c}(\rho, \nu) \quad \text{with} \quad \tilde{c}(\rho, \nu) = \sqrt{(1 - \alpha)\nu^2 + \alpha \frac{p'(\rho) - a(t)}{\epsilon^2}}. \quad (5)$$

The wave speeds $\tilde{\lambda}_{\pm}(\rho, \nu)$ are real for all $\nu \in \mathbb{R}$ and $\rho > 0$ as soon as

$$a(t) \leq \min_{x \in \Omega} \{p'(\rho(x, t))\}.$$

The system is thus hyperbolic under this condition. It may seem natural to simply set

$$a(t) = \min_{x \in \Omega} \{p'(\rho(x, t))\}. \quad (6)$$

But, with this choice, spurious oscillations are observed in some test cases for large values of ϵ . They appear in regions where the density is nearly uniform and the material velocity vanishes. Indeed, in these regions, the corresponding sound speed vanishes and the spurious oscillations are probably due to a lack of numerical diffusion in the Slow Dynamic part of the splitting. To overcome this difficulty, in these test cases (see Section 3.2), we set

$$a(t) = \min_{x \in \Omega} \{p'(\rho(x, t))\} - \iota(t)\epsilon^2 > 0, \quad (7)$$

where $\iota(t)$ is a constant smaller than the minimum of p' (so that $a(t) \geq \iota(t)(1 - \epsilon^2) > 0$ for $\epsilon < 1$). In the numerical tests of Section 3.2, we simply choose $\iota(t) = 0$ or $\iota(t) = 1$ when additional numerical diffusion is needed for large ϵ .

The choice of the splitting parameter α might impact the stability of the scheme: [38] prove that, for a linearized version of the system when $0 < \epsilon \ll 1$, choosing $\alpha \in (0, \frac{1}{2})$ ensures the stability (in a sense defined in [33], see also [35, 38]) of the above splitting when it is combined with Rusanov-type numerical fluxes. In [20], the numerical experiments are performed with $\alpha = \epsilon^2$. As detailed below, we also find advantages in adopting this choice. It leads to

$$\tilde{\lambda}_{\pm}(\rho, \nu) = \nu \pm \sqrt{(1 - \epsilon^2)\nu^2 + p'(\rho) - a(t)}.$$

and consequently since $a(t) > 0$, we have

$$[\tilde{\lambda}_{\pm}(\rho, \nu)]^{\pm} \leq 2\nu^{\pm} + \sqrt{p'(\rho)}, \quad (8)$$

where the notation $[\cdot]^{\pm}$ is defined by $[x]^{\pm} = (|x| \pm x)/2$, $\forall x \in \mathbb{R}$. Whereas the wave speeds of the original system (1) behave like $\nu \pm \sqrt{p'(\rho)}/\epsilon$ (as recalled in the introduction), we observe that the wave speeds of the system (SD) remain bounded when ϵ goes to 0 and thus ensures unconstrained CFL conditions with respect to ϵ (see Proposition 2.4).

Remark 2.1. As emphasized in [20], the choice (6) ensures also that wave speeds of the system (SD) remain bounded when ϵ goes to 0 whatever the value of α . Indeed, if the initial conditions are well-prepared, we have

$$\frac{\alpha}{\epsilon^2} \left(p'(\rho) - \min_{x \in \Omega} \{ p'(\rho(x, t)) \} \right) = \alpha \left(\rho^{(2)}(t, x) - \min_{x \in \Omega} \{ \rho^{(2)}(t, x) \} \right) p''(\rho^{(0)}) + \mathcal{O}(\epsilon).$$

We now turn to the numerical resolution of those two systems. The characteristic speeds of the system (SD) are no longer stiff – in contrast to the wave speed of (1) – and it does not induce severe stability conditions. We shall make use of the space discretization set up in [3] for this system. The system (FD) is a simple linear hyperbolic system for the variable $(\rho, \mathbf{q} = \rho \mathbf{u})$. However, it is not clear whether a direct resolution of the system can preserve the positivity of the density, a property which is absolutely crucial for the stability of the whole procedure, and for physical purposes. For this reason, we shall treat (FD) as a non linear system (for variables ρ and \mathbf{u}) to be solved implicitly.

2.2 Time discretization and stability

From now on we use the following notation: given a quantity Q at the current time t we denote by \bar{Q} its update at the next time $t + \delta t$. Let us detail the scheme by using the explicit Euler scheme for (SD) and the implicit Euler scheme for (FD), which can be summarized in the semi-discrete form:

$$\begin{cases} \frac{\rho^* - \rho}{\delta t} + \alpha \nabla \cdot (\rho \mathbf{u}) = 0, \\ \frac{\rho^* \mathbf{u}^* - \rho \mathbf{u}}{\delta t} + \nabla \cdot (\rho \mathbf{u} \otimes \mathbf{u}) + \nabla \left(\frac{p(\rho) - a(t)\rho}{\epsilon^2} \right) = 0, \end{cases}$$

and

$$\begin{cases} \frac{\bar{\rho} - \rho^*}{\delta t} + (1 - \alpha) \nabla \cdot (\bar{\rho} \bar{\mathbf{u}}) = 0, \\ \frac{\bar{\rho} \bar{\mathbf{u}} - \rho^* \mathbf{u}^*}{\delta t} + \frac{a(t)}{\epsilon^2} \nabla \bar{\rho} = 0. \end{cases}$$

Remark 2.2. In [20], see also [34], the time discretization is constructed to reach second order accuracy: the two-level Adams-Bashforth scheme is used for the explicit slow system and the Crank-Nicolson scheme is used for the fast implicit system. Of course, it is straightforward to adapt such a time-discretization, but the analysis would be much more involved.

The construction proposed in [20] relies on the following stability statement for split systems, see [20, Lemma 3.1].

Lemma 2.3. *If both methods*

$$\frac{U^{n+1} - U^n}{\delta t} + AU^n = 0 \quad \text{and} \quad \frac{U^{n+1} - U^n}{\delta t} + BU^{n+1} = 0,$$

are L^2 -stable, then the following method is also L^2 -stable

$$\frac{U^{n+1} - U^n}{\delta t} + AU^n + BU^{n+1} = 0$$

in the sense that

$$\|U^n\|_{L^2} \leq e^{Cn\delta t} \|U^0\|_{L^2}$$

holds for a certain positive constant C .

Note however that this is a rough notion of stability. It gives an intuition on the relevance of the splitting. However, as said in introduction, it turns out that certain fast-slow splittings, that might look physically relevant at first sight with formal stability conditions independent of ϵ , give rise in practice to numerical instabilities. This is where the interplay between time and space discretizations arises: the origin of these instabilities is due to the checkerboard pressure profiles, a well-known difficulty in incompressible computational fluid mechanics. Since introducing stabilization terms in the scheme impacts the stability conditions and often leads to restriction depending on ϵ again, see in particular [34, sp. Section 3.5, Theorem 4.1 and Remark 4.2], we take advantages, in this article, of the use of staggered grids and its well-known stability properties in the incompressible regime. The stability properties of the full discrete scheme are further analysed in Section 2.4.

2.3 Space discretization

We detail the scheme in 2D for a Cartesian grid. The computational domain is the square

$$\Omega = [a_x, b_x] \times [a_y, b_y] \subset \mathbb{R}^2.$$

The discretization strategy adopts the principles of the MAC schemes [21], which are precisely suited to avoid the spurious modes in incompressible regimes. We proceed as follows:

- the primal mesh is given by subdividing each direction

$$\begin{aligned} a_x &= x_1 < x_2 < \dots < x_{i-1} < x_i < x_{i+1} < \dots < x_N < x_{N+1} = b_x, \\ a_y &= y_1 < y_2 < \dots < y_{j-1} < y_j < y_{j+1} < \dots < y_M < y_{M+1} = b_y. \end{aligned}$$

- Then, we define the midpoints

$$x_{i+1/2} = \frac{x_i + x_{i+1}}{2}, \quad \forall i \in \{1, \dots, N\}, \quad \text{and} \quad y_{j+1/2} = \frac{y_j + y_{j+1}}{2}, \quad \forall j \in \{1, \dots, M\}.$$

- We denote by $\delta x_{i+1/2}$, $\delta y_{j+1/2}$, δx_i and δy_j the length of $[x_i, x_{i+1}]$, $[y_j, y_{j+1}]$, $[x_{i-1/2}, x_{i+1/2}]$ and $[y_{j-1/2}, y_{j+1/2}]$ respectively. We also denote by $h = \max(\max_i \delta x_{i+1/2}, \max_j \delta y_{j+1/2})$ the size of the mesh.

The discrete densities, the horizontal and the vertical velocities are stored at different locations, see Fig. 1:

- the density ρ is evaluated at the centers $(x_{i+1/2}, y_{j+1/2})$ of the primal cells: the corresponding numerical unknowns are denoted by $\rho_{i+1/2, j+1/2}$,
- the horizontal velocity u is evaluated on the vertical edges of the primal cells, at point $(x_i, y_{j+1/2})$: the numerical unknowns thus read $u_{i, j+1/2}$
- the vertical velocity v is evaluated on the horizontal edges of the primal cells, at point $(x_{i+1/2}, y_j)$: the numerical unknowns thus read $v_{i+1/2, j}$.

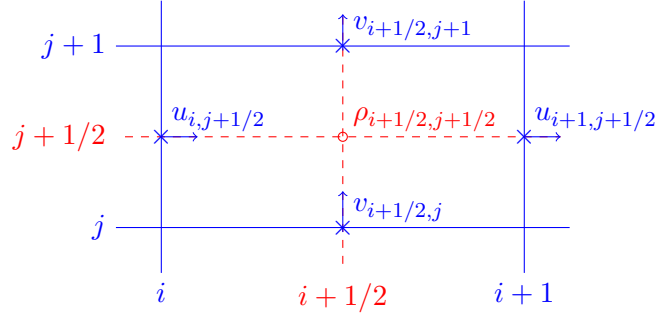


Figure 1: Position of the unknowns on a MAC grid

The density can be naturally defined at the edges of the primal mesh by averaging as follows

$$\rho_{i, j+\frac{1}{2}} = \frac{\delta x_{i+\frac{1}{2}} \rho_{i+\frac{1}{2}, j+\frac{1}{2}} + \delta x_{i-\frac{1}{2}} \rho_{i-\frac{1}{2}, j+\frac{1}{2}}}{2\delta x_i},$$

$$\rho_{i+\frac{1}{2}, j} = \frac{\delta y_{j+\frac{1}{2}} \rho_{i+\frac{1}{2}, j+\frac{1}{2}} + \delta y_{j-\frac{1}{2}} \rho_{i+\frac{1}{2}, j-\frac{1}{2}}}{2\delta y_j}.$$

Indeed, the different sets of unknowns can be thought of as piecewise constant functions on different meshes: the primal unknowns $\rho_{i+\frac{1}{2}, j+\frac{1}{2}}$ can be considered as constant on primal cells $[x_i, x_{i+1}] \times [y_j, y_{j+1}]$ whereas the dual unknowns $\rho_{i, j+\frac{1}{2}}$, resp. $\rho_{i+\frac{1}{2}, j}$, can be considered as constant on dual cells $[x_{i-\frac{1}{2}}, x_{i+\frac{1}{2}}] \times [y_j, y_{j+1}]$, resp. $[x_i, x_{i+1}] \times [y_{j-\frac{1}{2}}, y_{j+\frac{1}{2}}]$. The above definitions of $\rho_{i, j+\frac{1}{2}}$, resp. $\rho_{i+\frac{1}{2}, j}$, ensure that the integral of the discrete densities over the dual cell $[x_{i-\frac{1}{2}}, x_{i+\frac{1}{2}}] \times [y_j, y_{j+1}]$, resp. $[x_i, x_{i+1}] \times [y_{j-\frac{1}{2}}, y_{j+\frac{1}{2}}]$, is the same whatever the considered set of unknowns (that is the primal unknowns $\rho_{i+\frac{1}{2}, j+\frac{1}{2}}$ or the dual unknowns $\rho_{i, j+\frac{1}{2}}$, resp. $\rho_{i+\frac{1}{2}, j}$). These expressions are different from linear interpolation but bearing in mind that $x_{i+\frac{1}{2}}$ is the midpoint of $[x_i, x_{i+1}]$, we have $\delta x_{i-\frac{1}{2}} + \delta x_{i+\frac{1}{2}} = 2\delta x_i$ (and similarly $\delta y_{j-\frac{1}{2}} + \delta y_{j+\frac{1}{2}} = 2\delta y_j$) so that $\rho_{i, j+\frac{1}{2}}$ and $\rho_{i+\frac{1}{2}, j}$ are convex combinations of the densities stored at the centers of the primal cells.

We solve (SD) in order to produce an intermediate solution $(\rho_{i+1/2, j+1/2}^*, u_{i, j+1/2}^*, v_{i+1/2, j}^*)$

with the following scheme

$$\left\{ \begin{array}{l} \frac{\rho_{i+\frac{1}{2},j+\frac{1}{2}}^* - \rho_{i+\frac{1}{2},j+\frac{1}{2}}}{\delta t} + \alpha \left(\frac{\mathcal{F}_{i+1,j+\frac{1}{2}}^x - \mathcal{F}_{i,j+\frac{1}{2}}^x}{\delta x_{i+\frac{1}{2}}} + \frac{\mathcal{F}_{i+\frac{1}{2},j+1}^y - \mathcal{F}_{i+\frac{1}{2},j}^y}{\delta y_{j+\frac{1}{2}}} \right) = 0, \\ \frac{\rho_{i,j+\frac{1}{2}}^* u_{i,j+\frac{1}{2}}^* - \rho_{i,j+\frac{1}{2}} u_{i,j+\frac{1}{2}}}{\delta t} + \frac{\mathcal{G}_{i+\frac{1}{2},j+\frac{1}{2}}^{u,x} - \mathcal{G}_{i-\frac{1}{2},j+\frac{1}{2}}^{u,x}}{\delta x_i} \\ \quad + \frac{\mathcal{G}_{i,j+1}^{u,y} - \mathcal{G}_{i,j}^{u,y}}{\delta y_{j+\frac{1}{2}}} + \frac{\Pi_{i+\frac{1}{2},j+\frac{1}{2}} - \Pi_{i-\frac{1}{2},j+\frac{1}{2}}}{\delta x_i} = 0, \quad (\text{SDd}) \\ \frac{\rho_{i+\frac{1}{2},j}^* v_{i+\frac{1}{2},j}^* - \rho_{i+\frac{1}{2},j} v_{i+\frac{1}{2},j}}{\delta t} + \frac{\mathcal{G}_{i+1,j}^{v,x} - \mathcal{G}_{i,j}^{v,x}}{\delta x_{i+\frac{1}{2}}} \\ \quad + \frac{\mathcal{G}_{i+\frac{1}{2},j+\frac{1}{2}}^{v,y} - \mathcal{G}_{i+\frac{1}{2},j-\frac{1}{2}}^{v,y}}{\delta y_j} + \frac{\Pi_{i+\frac{1}{2},j+\frac{1}{2}} - \Pi_{i+\frac{1}{2},j-\frac{1}{2}}}{\delta y_j} = 0, \end{array} \right.$$

where we are going to define the numerical fluxes in these formulae. The system (SD) differs from the usual Euler system. Nevertheless, we can readily adapt the scheme proposed in [3, 31]. Bearing in mind that the sound speed $\tilde{c}(\rho, \nu)$ defined in (5) now depends on ρ and ν a velocity component u or v , we get the following definition for the fluxes. We introduce

$$\mathcal{F}^+(\rho, \nu) = \begin{cases} 0 & \text{if } \nu \leq -\tilde{c}(\rho, \nu), \\ \frac{\rho}{4\tilde{c}(\rho, \nu)} (\nu + \tilde{c}(\rho, \nu))^2 & \text{if } |\nu| \leq \tilde{c}(\rho, \nu), \\ \rho\nu & \text{if } \nu \geq \tilde{c}(\rho, \nu), \end{cases}$$

and

$$\mathcal{F}^-(\rho, \nu) = \begin{cases} \rho\nu & \text{if } \nu \leq -\tilde{c}(\rho, \nu), \\ -\frac{\rho}{4\tilde{c}(\rho, \nu)} (\nu - \tilde{c}(\rho, \nu))^2 & \text{if } |\nu| \leq \tilde{c}(\rho, \nu), \\ 0 & \text{if } \nu \geq \tilde{c}(\rho, \nu). \end{cases}$$

Note that, with this convention, we have $\pm\mathcal{F}^\pm(\rho, \nu) \geq 0$. Then we set

$$\mathcal{F}_{i,j+\frac{1}{2}}^x = \mathcal{F}_{i,j+\frac{1}{2}}^{x,+} + \mathcal{F}_{i,j+\frac{1}{2}}^{x,-} \quad \text{and} \quad \mathcal{F}_{i+\frac{1}{2},j}^y = \mathcal{F}_{i+\frac{1}{2},j}^{y,+} + \mathcal{F}_{i+\frac{1}{2},j}^{y,-},$$

with

$$\begin{aligned} \mathcal{F}_{i,j+\frac{1}{2}}^{x,+} &= \mathcal{F}^+(\rho_{i-\frac{1}{2},j+\frac{1}{2}}, u_{i,j+\frac{1}{2}}) & \text{and} & \quad \mathcal{F}_{i,j+\frac{1}{2}}^{x,-} = \mathcal{F}^-(\rho_{i+\frac{1}{2},j+\frac{1}{2}}, u_{i,j+\frac{1}{2}}), \\ \mathcal{F}_{i+\frac{1}{2},j}^{y,+} &= \mathcal{F}^+(\rho_{i+\frac{1}{2},j-\frac{1}{2}}, v_{i+\frac{1}{2},j}) & \text{and} & \quad \mathcal{F}_{i+\frac{1}{2},j}^{y,-} = \mathcal{F}^-(\rho_{i+\frac{1}{2},j+\frac{1}{2}}, v_{i+\frac{1}{2},j}). \end{aligned}$$

The definition of the convection fluxes in the momentum equation is given by

$$\mathcal{G}_{i+\frac{1}{2},j+\frac{1}{2}}^{u,x} = u_{i,j+\frac{1}{2}} \mathcal{F}_{i+\frac{1}{2},j+\frac{1}{2}}^{x,+} + u_{i+1,j+\frac{1}{2}} \mathcal{F}_{i+\frac{1}{2},j+\frac{1}{2}}^{x,-} \quad \text{and} \quad \mathcal{G}_{i,j}^{u,y} = u_{i,j-\frac{1}{2}} \mathcal{F}_{i,j}^{y,+} + u_{i,j+\frac{1}{2}} \mathcal{F}_{i,j}^{y,-}$$

and a similar definition for $\mathcal{G}_{i,j}^{v,x}$ and $\mathcal{G}_{i+\frac{1}{2},j+\frac{1}{2}}^{v,y}$. It uses the averaged mass fluxes

$$\mathcal{F}_{i+\frac{1}{2},j+\frac{1}{2}}^{x,\pm} = \frac{1}{2} \left(\mathcal{F}_{i,j+\frac{1}{2}}^{x,\pm} + \mathcal{F}_{i+1,j+\frac{1}{2}}^{x,\pm} \right) \quad \text{and} \quad \mathcal{F}_{i,j}^{y,\pm} = \frac{\delta x_{i+\frac{1}{2}} \mathcal{F}_{i+\frac{1}{2},j}^{y,\pm} + \delta x_{i-\frac{1}{2}} \mathcal{F}_{i-\frac{1}{2},j}^{y,\pm}}{2\delta x_i}.$$

The discrete analog of the parameter a in (7) is the discrete quantity

$$a_d = \min_{i,j} \left\{ p'(\rho_{i+\frac{1}{2},j+\frac{1}{2}}) \right\} - \iota \epsilon^2, \quad (9)$$

and thus the pressure term $\Pi_{i+\frac{1}{2},j+\frac{1}{2}}$ – which differs from the usual Euler case dealt with in [3] – is defined by

$$\Pi_{i+\frac{1}{2},j+\frac{1}{2}} = \frac{p(\rho_{i+\frac{1}{2},j+\frac{1}{2}}) - a_d \rho_{i+\frac{1}{2},j+\frac{1}{2}}}{\epsilon^2}.$$

We now turn to the resolution of the system (FD) to find $(\bar{\rho}_{i+\frac{1}{2},j+\frac{1}{2}}, \bar{u}_{i,j+\frac{1}{2}}, \bar{v}_{i+\frac{1}{2},j})$, using the solution of (SDd) we have just obtained as initial data. Working on staggered grids offers us the possibility to use a centered scheme for the gradient of the pressure term, which is the key to overcome the difficulties recorded with methods on colocalized meshes, see [10, 34]. We set

$$\left\{ \begin{array}{l} \frac{\bar{\rho}_{i+\frac{1}{2},j+\frac{1}{2}} - \rho_{i+\frac{1}{2},j+\frac{1}{2}}^*}{\delta t} + (1 - \alpha) \left(\frac{\overline{\mathcal{F}}_{i+1,j+\frac{1}{2}}^{Up,x} - \overline{\mathcal{F}}_{i,j+\frac{1}{2}}^{Up,x}}{\delta x_{i+\frac{1}{2}}} + \frac{\overline{\mathcal{F}}_{i+\frac{1}{2},j+1}^{Up,y} - \overline{\mathcal{F}}_{i+\frac{1}{2},j}^{Up,y}}{\delta y_{j+\frac{1}{2}}} \right) = 0, \\ \frac{\bar{\rho}_{i,j+\frac{1}{2}} \bar{u}_{i,j+\frac{1}{2}} - \rho_{i,j+\frac{1}{2}}^* u_{i,j+\frac{1}{2}}^*}{\delta t} + \frac{a_d \bar{\rho}_{i+\frac{1}{2},j+\frac{1}{2}} - \bar{\rho}_{i-\frac{1}{2},j+\frac{1}{2}}}{\epsilon^2 \delta x_i} = 0, \\ \frac{\bar{\rho}_{i+\frac{1}{2},j} \bar{v}_{i+\frac{1}{2},j} - \rho_{i+\frac{1}{2},j}^* v_{i+\frac{1}{2},j}^*}{\delta t} + \frac{a_d \bar{\rho}_{i+\frac{1}{2},j+\frac{1}{2}} - \bar{\rho}_{i+\frac{1}{2},j-\frac{1}{2}}}{\epsilon^2 \delta y_j} = 0. \end{array} \right. \quad (\text{FDd})$$

The upwind fluxes $\overline{\mathcal{F}}^{Up,x}$ and $\overline{\mathcal{F}}^{Up,y}$ are obtained by applying the upwinding principle based on the sign of the velocity. Precisely, we use in (FDd) the following *implicit* fluxes

$$\overline{\mathcal{F}}_{i,j+\frac{1}{2}}^{Up,x} = \bar{\rho}_{i-\frac{1}{2},j+\frac{1}{2}} [\bar{u}_{i,j+\frac{1}{2}}]^+ - \bar{\rho}_{i+\frac{1}{2},j+\frac{1}{2}} [\bar{u}_{i,j+\frac{1}{2}}]^-$$

and

$$\overline{\mathcal{F}}_{i+\frac{1}{2},j}^{Up,y} = \bar{\rho}_{i+\frac{1}{2},j-\frac{1}{2}} [\bar{v}_{i+\frac{1}{2},j}]^+ - \bar{\rho}_{i+\frac{1}{2},j+\frac{1}{2}} [\bar{v}_{i+\frac{1}{2},j}]^-.$$

Here, we are still using the definition $[x]^\pm = (|x| \pm x)/2$, $\forall x \in \mathbb{R}$. In contrast to [20], we are working here on staggered grids and the resolution does not involve the momentum as a numerical unknown but instead the velocity. Despite the fact that (FD) is a linear system for the conservative quantities $(\rho, q = \rho \mathbf{u})$, the corresponding discrete equation (FDd) becomes a nonlinear problem for the non-conservative variables. Accordingly, the update does not come from the resolution of a linear system, and, instead, we have to use a root-finding algorithm as the Newton-Raphson method. This is absolutely crucial in order to preserve the positivity of the density (stated below, see Proposition 2.4). Nevertheless, it is important to note that, even if the system looks fully implicit, the expressions for $\bar{u}_{i,j+\frac{1}{2}}$ and $\bar{v}_{i+\frac{1}{2},j}$ as a function of $\bar{\rho}_{i+\frac{1}{2},j+\frac{1}{2}}$ can be readily obtained from the last two equations of (FDd) so that the system can be solved as a non linear system of scalar equations involving only the unknowns $(\bar{\rho}_{i+\frac{1}{2},j+\frac{1}{2}})$ with $i \in \{1, \dots, N\}$, $j \in \{1, \dots, M\}$. This is of great importance to save computational cost.

In terms of stability let us give the following statement, which justifies that the scheme produces physically relevant quantities with a stability condition that does not degenerate when ϵ becomes small.

Proposition 2.4. *We set $\alpha = \epsilon^2$. Suppose that the data (ρ, \mathbf{u}) is well-prepared, in the sense of Definition 2.6 and such that $\rho_{j+\frac{1}{2}} \geq 0$ for all j . We assume the following CFL-like condition*

$$\begin{aligned} \frac{\delta t}{\delta x_{i+\frac{1}{2}}} \left([u_{i,j+\frac{1}{2}}]^- + [u_{i+1,j+\frac{1}{2}}]^+ + \sqrt{p'(\rho_{i+\frac{1}{2},j+\frac{1}{2}})} \right) \\ + \frac{\delta t}{\delta y_{j+\frac{1}{2}}} \left([v_{i+\frac{1}{2},j}]^- + [v_{i+\frac{1}{2},j+1}]^+ + \sqrt{p'(\rho_{i+\frac{1}{2},j+\frac{1}{2}})} \right) \leq \frac{1}{2}, \end{aligned} \quad (10)$$

then the scheme preserves the non-negativity of the density: $\bar{\rho}_{j+\frac{1}{2}} \geq 0$ for all j .

Proof. We adapt readily the arguments in [31] to justify that (SDd) preserves positive densities, under the following CFL-like condition

$$\begin{aligned} \frac{\delta t}{\delta x_{i+\frac{1}{2}}} \left([\tilde{\lambda}_-(\rho_{i+\frac{1}{2},j+\frac{1}{2}}, u_{i,j+\frac{1}{2}})]^- + [\tilde{\lambda}_+(\rho_{i+\frac{1}{2},j+\frac{1}{2}}, u_{i+1,j+\frac{1}{2}})]^+ \right) \\ + \frac{\delta t}{\delta y_{j+\frac{1}{2}}} \left([\tilde{\lambda}_-(\rho_{i+\frac{1}{2},j+\frac{1}{2}}, v_{i+\frac{1}{2},j})]^- + [\tilde{\lambda}_+(\rho_{i+\frac{1}{2},j+\frac{1}{2}}, v_{i+\frac{1}{2},j+1})]^+ \right) \leq 1. \end{aligned}$$

Owing to (8) which holds since $\alpha = \epsilon^2$, this condition is ensured when (10) is satisfied. Thus, it proves that $\rho_{i+\frac{1}{2},j+\frac{1}{2}}^* > 0$ for all i, j . We now turn to the resolution of the Fast Dynamics (FDd). The monotonicity of the implicit Upwind scheme [6] ensures that $\bar{\rho}_{i+\frac{1}{2},j+\frac{1}{2}} > 0$ as soon as $\rho_{i+\frac{1}{2},j+\frac{1}{2}}^* > 0$. We conclude that $\rho_{i+\frac{1}{2},j+\frac{1}{2}} > 0$ at every time step under the CFL-like condition (10). □

2.4 Low Mach regimes and AP-scheme

We wish now to show that the scheme performs well in low Mach regimes and exhibits the AP features. Let us suppose that the initial data of the system are well prepared in the sense of Definition 1.1. As said above, the solutions of the compressible Euler system (1) converge to a constant density and a velocity field solution of the Incompressible Euler system (3). Our purpose is two-fold:

- 1) to show that our solver automatically becomes an incompressible solver for (3) in the low Mach number regime $0 < \epsilon \ll 1$. It makes the AP character of the scheme precise.
- 2) to justify that the scheme preserves well prepared data, in the discrete sense given in Definition 2.6 below. This crucial property justifies that the proposed discretization does not produce spurious oscillations that can prevent to capture the correct solution in low Mach regimes, see [9, 10, 12, 19, 17, 34].

In order to bring out that the behaviour of the continuous case is well reproduced, we introduce an ansatz of the discrete solution:

- $\rho_{i+\frac{1}{2},j+\frac{1}{2}} = \rho_{i+\frac{1}{2},j+\frac{1}{2}}^{(0)} + \epsilon \rho_{i+\frac{1}{2},j+\frac{1}{2}}^{(1)} + \epsilon^2 \rho_{i+\frac{1}{2},j+\frac{1}{2}}^{(2)} + \dots$
- $u_{i,j+\frac{1}{2}} = u_{i,j+\frac{1}{2}}^{(0)} + \epsilon u_{i,j+\frac{1}{2}}^{(1)} + \epsilon^2 u_{i,j+\frac{1}{2}}^{(2)} + \dots$ and $v_{i+\frac{1}{2},j} = v_{i+\frac{1}{2},j}^{(0)} + \epsilon v_{i+\frac{1}{2},j}^{(1)} + \epsilon^2 v_{i+\frac{1}{2},j}^{(2)} + \dots$
- $p_{i+\frac{1}{2},j+\frac{1}{2}} = p_{i+\frac{1}{2},j+\frac{1}{2}}^{(0)} + \epsilon p_{i+\frac{1}{2},j+\frac{1}{2}}^{(1)} + \epsilon^2 p_{i+\frac{1}{2},j+\frac{1}{2}}^{(2)} + \dots$

The investigation of the asymptotic regime $\epsilon \rightarrow 0$ will make the following discrete operators appear.

Definition 2.5. We define the discrete divergence operator $\nabla_d \cdot$ of a vector $\mathbf{u} = (u, v)$ as

$$\nabla_d \cdot \mathbf{u}_{i+\frac{1}{2}, j+\frac{1}{2}} = \frac{u_{i+1, j+\frac{1}{2}} - u_{i, j+\frac{1}{2}}}{\delta x_{i+\frac{1}{2}}} + \frac{v_{i+\frac{1}{2}, j+1} - v_{i+\frac{1}{2}, j}}{\delta y_{j+\frac{1}{2}}},$$

and the discrete Laplacian operator Δ_d of a scalar quantity p as

$$\begin{aligned} \Delta_d p_{i+\frac{1}{2}, j+\frac{1}{2}} &= \frac{1}{\delta x_{i+\frac{1}{2}}} \left(\frac{p_{i+\frac{3}{2}, j+\frac{1}{2}} - p_{i+\frac{1}{2}, j+\frac{1}{2}}}{\delta x_{i+1}} - \frac{p_{i+\frac{1}{2}, j+\frac{1}{2}} - p_{i-\frac{1}{2}, j+\frac{1}{2}}}{\delta x_i} \right) \\ &+ \frac{1}{\delta y_{j+\frac{1}{2}}} \left(\frac{p_{i+\frac{1}{2}, j+\frac{3}{2}} - p_{i+\frac{1}{2}, j+\frac{1}{2}}}{\delta y_{j+1}} - \frac{p_{i+\frac{1}{2}, j+\frac{1}{2}} - p_{i+\frac{1}{2}, j-\frac{1}{2}}}{\delta y_j} \right). \end{aligned}$$

Since the preparation of data is an important assumption for the analysis of the asymptotic behaviour, it is convenient to introduce an equivalent definition at the discrete level.

Definition 2.6. Discrete data $(\rho, \mathbf{u} = (u, v))$ are said to be well-prepared if they satisfy, for all i, j ,

- $\rho_{i+\frac{1}{2}, j+\frac{1}{2}} = \rho^{(0)} + \epsilon \rho^{(1)} + \mathcal{O}(\epsilon^2)$ with $\rho^{(0)}, \rho^{(1)}$ real constants,
- $\nabla_d \cdot \mathbf{u}_{i+\frac{1}{2}, j+\frac{1}{2}}^{(0)} = 0$, and thus $\nabla_d \cdot \mathbf{u}_{i+\frac{1}{2}, j+\frac{1}{2}} = \mathcal{O}(\epsilon)$.

This definition appeared in [9, 10, 12]; it plays a crucial role in the analysis of the sensitivity of numerical solvers to the grid geometry. It is the discrete counterpart of Definition 1.1.

Let us suppose that the discrete solution is well-prepared in the sense of Definition 2.6 from time $t = 0$ up to time $t > 0$. We wish to show that the updated physical quantities still satisfy the conditions of Definition 2.6.

The first thing to notice is that the explicit pressure term drops out, as the modified explicit pressure has a simple expansion for small ϵ 's.

Lemma 2.7. *Let (ρ, \mathbf{u}) be well-prepared. The modified pressure $p(\rho) - a_d \rho$ in (SDd) admits the expansion*

$$\Pi_{i+\frac{1}{2}, j+\frac{1}{2}} := \frac{p(\rho_{i+\frac{1}{2}, j+\frac{1}{2}}) - a_d \rho_{i+\frac{1}{2}, j+\frac{1}{2}}}{\epsilon^2} = \frac{C_{-2}}{\epsilon^2} + \frac{C_{-1}}{\epsilon} + C_0 + \mathcal{O}(\epsilon)$$

where the coefficients C_{-2}, C_{-1}, C_0 do not depend on the considered cell.

Proof. Since the data are well-prepared, the pressure $p_{i+\frac{1}{2}, j+\frac{1}{2}} = p(\rho_{i+\frac{1}{2}, j+\frac{1}{2}})$ expands as

$$p_{i+\frac{1}{2}, j+\frac{1}{2}} = p(\rho^{(0)}) + \epsilon \rho^{(1)} p'(\rho^{(0)}) + \epsilon^2 \left(\rho_{i+\frac{1}{2}, j+\frac{1}{2}}^{(2)} p'(\rho^{(0)}) + \frac{\rho^{(1)2}}{2} p''(\rho^{(0)}) \right) + \mathcal{O}(\epsilon^3). \quad (11)$$

Hence we obtain

$$\begin{aligned} \frac{p_{i+\frac{1}{2}, j+\frac{1}{2}} - a_d \rho_{i+\frac{1}{2}, j+\frac{1}{2}}}{\epsilon^2} &= \frac{p(\rho^{(0)}) - a_d^{(0)} \rho^{(0)}}{\epsilon^2} + \frac{\rho^{(1)} p'(\rho^{(0)}) - a_d^{(0)} \rho^{(1)} - a_d^{(1)} \rho^{(0)}}{\epsilon} \\ &+ \left(\rho_{i+\frac{1}{2}, j+\frac{1}{2}}^{(2)} p'(\rho^{(0)}) + \frac{\rho^{(1)2}}{2} p''(\rho^{(0)}) - a_d^{(0)} \rho_{i+\frac{1}{2}, j+\frac{1}{2}}^{(2)} - a_d^{(1)} \rho^{(1)} - a_d^{(2)} \rho^{(0)} \right) + \mathcal{O}(\epsilon). \end{aligned}$$

An expansion of the coefficient $a_d = \min_{i,j} p'(\rho_{i+\frac{1}{2},j+\frac{1}{2}}) - \iota\epsilon^2$:

$$a_d^{(0)} = p'(\rho^{(0)}), \quad a_d^{(1)} = \rho^{(1)} p''(\rho^{(0)}), \quad a_d^{(2)} = \min_{i,j} \left\{ \rho_{i+\frac{1}{2},j+\frac{1}{2}}^{(2)} \right\} p''(\rho^{(0)}) + \frac{\rho^{(1)2}}{2} p'''(\rho^{(0)}) - \iota, \quad (12)$$

leads to the conclusion with the following expressions of the constants C_{-2} , C_{-1} , C_0

$$\begin{aligned} C_0 &= -\frac{\rho^{(1)2}}{2} \left(p''(\rho^{(0)}) + \rho^{(0)} p'''(\rho^{(0)}) \right) - \min_{i,j} \left\{ \rho_{i+\frac{1}{2},j+\frac{1}{2}}^{(2)} \right\} p''(\rho^{(0)}) + \iota \rho^{(0)}, \\ C_{-1} &= -\rho^{(0)} \rho^{(1)} p''(\rho^{(0)}), \\ C_{-2} &= p(\rho^{(0)}) - \rho^{(0)} p'(\rho^{(0)}). \end{aligned}$$

□

As we did for the continuous system, we now insert the expansion in the scheme obtained by taking the sum of (SDd) and (FDd)

$$\begin{aligned} \frac{\bar{\rho}_{i+\frac{1}{2},j+\frac{1}{2}} - \rho_{i+\frac{1}{2},j+\frac{1}{2}}}{\delta t} + \alpha \left(\frac{\mathcal{F}_{i+1,j+\frac{1}{2}}^x - \mathcal{F}_{i,j+\frac{1}{2}}^x}{\delta x_{i+\frac{1}{2}}} + \frac{\mathcal{F}_{i+\frac{1}{2},j+1}^y - \mathcal{F}_{i+\frac{1}{2},j}^y}{\delta y_{j+\frac{1}{2}}} \right) \\ + (1-\alpha) \left(\frac{\bar{\mathcal{F}}_{i+1,j+\frac{1}{2}}^{Up,x} - \bar{\mathcal{F}}_{i,j+\frac{1}{2}}^{Up,x}}{\delta x_{i+\frac{1}{2}}} + \frac{\bar{\mathcal{F}}_{i+\frac{1}{2},j+1}^{Up,y} - \bar{\mathcal{F}}_{i+\frac{1}{2},j}^{Up,y}}{\delta y_{j+\frac{1}{2}}} \right) = 0, \end{aligned} \quad (13)$$

$$\begin{aligned} \frac{\bar{\rho}_{i,j+\frac{1}{2}} \bar{u}_{i,j+\frac{1}{2}} - \rho_{i,j+\frac{1}{2}} u_{i,j+\frac{1}{2}}}{\delta t} + \frac{\mathcal{G}_{i+\frac{1}{2},j+\frac{1}{2}}^{u,x} - \mathcal{G}_{i-\frac{1}{2},j+\frac{1}{2}}^{u,x}}{\delta x_i} + \frac{\mathcal{G}_{i,j+1}^{u,y} - \mathcal{G}_{i,j}^{u,y}}{\delta y_{j+\frac{1}{2}}} \\ + \frac{\Pi_{i+\frac{1}{2},j+\frac{1}{2}} - \Pi_{i-\frac{1}{2},j+\frac{1}{2}}}{\delta x_i} + \frac{a_d \bar{\rho}_{i+\frac{1}{2},j+\frac{1}{2}} - \bar{\rho}_{i-\frac{1}{2},j+\frac{1}{2}}}{\epsilon^2 \delta x_i} = 0, \end{aligned} \quad (14)$$

$$\begin{aligned} \frac{\bar{\rho}_{i+\frac{1}{2},j} \bar{v}_{i+\frac{1}{2},j} - \rho_{i+\frac{1}{2},j} v_{i+\frac{1}{2},j}}{\delta t} + \frac{\mathcal{G}_{i+1,j}^{v,x} - \mathcal{G}_{i,j}^{v,x}}{\delta x_{i+\frac{1}{2}}} + \frac{\mathcal{G}_{i+\frac{1}{2},j+\frac{1}{2}}^{v,y} - \mathcal{G}_{i+\frac{1}{2},j-\frac{1}{2}}^{v,y}}{\delta y_j} \\ + \frac{\Pi_{i+\frac{1}{2},j+\frac{1}{2}} - \Pi_{i+\frac{1}{2},j-\frac{1}{2}}}{\delta y_j} + \frac{a_d \bar{\rho}_{i+\frac{1}{2},j+\frac{1}{2}} - \bar{\rho}_{i+\frac{1}{2},j-\frac{1}{2}}}{\epsilon^2 \delta y_j} = 0, \end{aligned} \quad (15)$$

and we identify terms arising with the same power of ϵ .

- 1) The leading order term in the momentum equations (14) and (15) scales as $\mathcal{O}\left(\frac{1}{\epsilon^2}\right)$. It comes from the pressure gradient. However, owing to Lemma 2.7, the explicit pressure gradient defined from $\Pi_{i+\frac{1}{2},j+\frac{1}{2}}$ contains only $\mathcal{O}(\epsilon)$ terms. It leads to

$$\frac{\bar{\rho}_{i+\frac{1}{2},j+\frac{1}{2}}^{(0)} - \bar{\rho}_{i-\frac{1}{2},j+\frac{1}{2}}^{(0)}}{\delta x_i} = 0 \quad \text{and} \quad \frac{\bar{\rho}_{i+\frac{1}{2},j+\frac{1}{2}}^{(0)} - \bar{\rho}_{i+\frac{1}{2},j-\frac{1}{2}}^{(0)}}{\delta y_j} = 0.$$

From this, we deduce that, for all (i,j) , $\bar{\rho}_{i-\frac{1}{2},j+\frac{1}{2}}^{(0)} = \bar{\rho}_{i+\frac{1}{2},j+\frac{1}{2}}^{(0)} = \bar{\rho}_{i+\frac{1}{2},j-\frac{1}{2}}^{(0)}$. In other words, at the discrete level the leading term in the updated density $\bar{\rho}^{(0)}$ is constant in space.

- 2) Then, at order $\mathcal{O}\left(\frac{1}{\epsilon}\right)$, we similarly get

$$\frac{\bar{\rho}_{i+\frac{1}{2},j+\frac{1}{2}}^{(1)} - \bar{\rho}_{i-\frac{1}{2},j+\frac{1}{2}}^{(1)}}{\delta x_i} = 0 \quad \text{and} \quad \frac{\bar{\rho}_{i+\frac{1}{2},j+\frac{1}{2}}^{(1)} - \bar{\rho}_{i+\frac{1}{2},j-\frac{1}{2}}^{(1)}}{\delta y_j} = 0.$$

We deduce that, for all (i, j) , $\bar{\rho}_{i-\frac{1}{2}, j+\frac{1}{2}}^{(1)} = \bar{\rho}_{i+\frac{1}{2}, j+\frac{1}{2}}^{(1)} = \bar{\rho}_{i+\frac{1}{2}, j-\frac{1}{2}}^{(1)}$: at the discrete level $\bar{\rho}^{(1)}$ is constant in space, too.

- 3) Let us now consider terms of order $\mathcal{O}(1)$. Since the data (ρ, \mathbf{u}) is assumed to be well-prepared, by multiplying the mass equation (13) by $\delta x_{i+\frac{1}{2}} \delta y_{j+\frac{1}{2}}$ and summing over i and j (with periodic or wall boundary conditions and denoting by N, M the number of grid points in the horizontal and vertical direction, respectively), we get

$$\sum_{j=1}^M \sum_{i=1}^N \delta x_{i+\frac{1}{2}} \delta y_{j+\frac{1}{2}} \frac{\bar{\rho}^{(0)} - \rho^{(0)}}{\delta t} = 0.$$

We remind the reader that $\sum_{j=1}^M \sum_{i=1}^N \delta x_{i+\frac{1}{2}} \delta y_{j+\frac{1}{2}} = |\Omega|$. Therefore $\bar{\rho}^{(0)} = \rho^{(0)}$: the discrete density at leading order is constant in space and time.

At the order $\mathcal{O}(1)$, since the density $\rho^{(0)}$ and the updated density $\bar{\rho}^{(0)}$ at leading order are constant in space and equal, the mass fluxes become

$$\mathcal{F}_{i,j+\frac{1}{2}}^{x,(0)} = \mathcal{F}^+(\rho^{(0)}, u_{i,j+\frac{1}{2}}^{(0)}) + \mathcal{F}^-(\rho^{(0)}, u_{i,j+\frac{1}{2}}^{(0)}) = \rho^{(0)} u_{i,j+\frac{1}{2}}^{(0)},$$

similarly $\mathcal{F}_{i+\frac{1}{2},j}^{y,(0)} = \rho^{(0)} v_{i+\frac{1}{2},j}^{(0)}$, $\bar{\mathcal{F}}_{i,j+\frac{1}{2}}^{Up,x} = \bar{\rho}^{(0)} \bar{u}_{i,j+\frac{1}{2}}^{(0)}$ and $\bar{\mathcal{F}}_{i+\frac{1}{2},j}^{Up,y} = \bar{\rho}^{(0)} \bar{v}_{i+\frac{1}{2},j}^{(0)}$. Going back to the discrete mass balance equation (13) it becomes at the order $\mathcal{O}(1)$

$$\alpha \rho^{(0)} \nabla_{\mathbf{d}} \cdot \mathbf{u}_{i+\frac{1}{2}, j+\frac{1}{2}}^{(0)} + (1 - \alpha) \rho^{(0)} \nabla_{\mathbf{d}} \cdot \bar{\mathbf{u}}_{i+\frac{1}{2}, j+\frac{1}{2}}^{(0)} = 0.$$

Since $\nabla_{\mathbf{d}} \cdot \mathbf{u}_{i+\frac{1}{2}, j+\frac{1}{2}}^{(0)}$ vanishes for all (i, j) , the update also satisfies $\nabla_{\mathbf{d}} \cdot \bar{\mathbf{u}}^{(0)} = 0$ and the second property in Definition 2.6 is preserved in the low Mach regime.

Remark 2.8. When the initial data $\mathbf{u}(x, 0) = \mathbf{u}^{\text{init}}(x)$ satisfies $\nabla \cdot \mathbf{u}^{\text{init},(0)}(x) = 0$ at the continuous level, the simple evaluation on the grid

$$\begin{aligned} \nabla_{\mathbf{d}} \cdot \mathbf{u}_{i+\frac{1}{2}, j+\frac{1}{2}}^{\text{init},(0)} &= \frac{u^{\text{init},(0)}(x_{i+1}, y_{j+\frac{1}{2}}) - u^{\text{init},(0)}(x_i, y_{j+\frac{1}{2}})}{\delta x_{i+\frac{1}{2}}} \\ &\quad + \frac{v^{\text{init},(0)}(x_{i+\frac{1}{2}}, y_{j+1}) - v^{\text{init},(0)}(x_{i+\frac{1}{2}}, y_j)}{\delta y_{j+\frac{1}{2}}} \end{aligned}$$

is of order $\mathcal{O}(h)$. This consistency error can propagate, and the obtained discrete velocity field is not discrete-divergence-free. In particular, if the mesh does not resolve the small scale ($\delta x \gg \epsilon$), the discrete initial data does not fulfill the criterion in Definition 2.6. Obviously, it is possible to adopt more involved definitions of $\mathbf{u}_{i+\frac{1}{2}, j+\frac{1}{2}}^{\text{init}}$, for instance based on a discrete Helmholtz decomposition to get rid of this issue but we can also take advantages to set

$$\alpha = \epsilon^2.$$

This choice, which already appears in [20], modifies the expansion above and the identification of the $\mathcal{O}(1)$ and $\mathcal{O}(\epsilon^2)$ terms in the discrete mass balance equation. In particular, with this choice, the method automatically projects the velocity onto the space of discrete-divergence-free fields when $\epsilon \rightarrow 0$: indeed, in this case, at the order $\mathcal{O}(1)$, the discrete mass balance equation becomes $\nabla_{\mathbf{d}} \cdot \bar{\mathbf{u}}_{i+\frac{1}{2}, j+\frac{1}{2}}^{(0)} = 0$.

- 4) At the order $\mathcal{O}(\epsilon)$, we multiply the mass equation (13) by $\delta x_{i+\frac{1}{2}} \delta y_{j+\frac{1}{2}}$ and sum for i, j and, since $\rho^{(1)}$ is a constant in space, we obtain that $\bar{\rho}^{(1)} = \rho^{(1)}$. The first property in Definition 2.6 is satisfied in the low Mach regime.

Remark 2.9. Using that $\bar{\rho}^{(k)} = \rho^{(k)}$ are constant for $k \in \{0, 1\}$, we can expand the mass flux $\mathcal{F}_{i,j+\frac{1}{2}}^x$ as

$$\begin{aligned} \mathcal{F}_{i,j+\frac{1}{2}}^x &= \mathcal{F}^+ \left(\rho^{(0)} + \epsilon \rho^{(1)}, u_{i,j+\frac{1}{2}}^{(0)} + \epsilon u_{i,j+\frac{1}{2}}^{(1)} \right) \\ &\quad + \mathcal{F}^- \left(\rho^{(0)} + \epsilon \rho^{(1)}, u_{i,j+\frac{1}{2}}^{(0)} + \epsilon u_{i,j+\frac{1}{2}}^{(1)} \right) + \mathcal{O}(\epsilon^2) \\ &= \left(\rho^{(0)} + \epsilon \rho^{(1)} \right) u_{i,j+\frac{1}{2}}^{(0)} + \epsilon \rho^{(0)} u_{i,j+\frac{1}{2}}^{(1)} + \mathcal{O}(\epsilon^2), \end{aligned}$$

so that we obtain the following expression

$$\mathcal{F}_{i,j+\frac{1}{2}}^{x,(1)} = \rho^{(1)} u_{i,j+\frac{1}{2}}^{(0)} + \rho^{(0)} u_{i,j+\frac{1}{2}}^{(1)}.$$

Similarly, we have

$$\begin{aligned} \mathcal{F}_{i+\frac{1}{2},j}^{y,(1)} &= \rho^{(1)} v_{i+\frac{1}{2},j}^{(0)} + \rho^{(0)} v_{i+\frac{1}{2},j}^{(1)}, \\ \overline{\mathcal{F}}_{i,j+\frac{1}{2}}^{Up,x,(1)} &= \rho^{(1)} \bar{u}_{i,j+\frac{1}{2}}^{(0)} + \rho^{(0)} \bar{u}_{i,j+\frac{1}{2}}^{(1)}, \\ \overline{\mathcal{F}}_{i+\frac{1}{2},j}^{Up,y,(1)} &= \rho^{(1)} \bar{v}_{i+\frac{1}{2},j}^{(0)} + \rho^{(0)} \bar{v}_{i+\frac{1}{2},j}^{(1)}. \end{aligned}$$

Thus, when $\alpha = \epsilon^2$, the first order term $\mathcal{O}(\epsilon)$ in the mass equation (13) reads:

$$\rho^{(1)} \nabla_d \cdot \bar{\mathbf{u}}_{i+1/2,j+1/2}^{(0)} + \rho^{(0)} \nabla_d \cdot \bar{\mathbf{u}}_{i+1/2,j+1/2}^{(1)} = 0.$$

Since, as said above in Remark 2.8, in this case we have $\nabla_d \cdot \bar{\mathbf{u}}^{(0)} = 0$, we conclude that $\nabla_d \cdot \bar{\mathbf{u}}^{(1)} = 0$, in analogy to the continuous case.

- 5) At the order $\mathcal{O}(1)$, using that $\rho^{(0)}$ and $\rho^{(1)}$ are constant, the momentum equation (14) gives us:

$$\begin{aligned} \rho^{(0)} \frac{\bar{u}_{i,j+\frac{1}{2}}^{(0)} - u_{i,j+\frac{1}{2}}^{(0)}}{\delta t} + \frac{\mathcal{G}_{i+\frac{1}{2},j+\frac{1}{2}}^{u,x,(0)} - \mathcal{G}_{i-\frac{1}{2},j+\frac{1}{2}}^{u,x,(0)}}{\delta x_i} \\ + \frac{\mathcal{G}_{i,j+1}^{u,y,(0)} - \mathcal{G}_{i,j}^{u,y,(0)}}{\delta y_{j+\frac{1}{2}}} + \frac{\bar{p}_{i+\frac{1}{2},j+\frac{1}{2}}^{(2)} - \bar{p}_{i-\frac{1}{2},j+\frac{1}{2}}^{(2)}}{\delta x_i} = 0, \end{aligned}$$

where $\bar{p}_{i+\frac{1}{2},j+\frac{1}{2}}^{(2)}$ is the $\mathcal{O}(\epsilon^2)$ term in the expansion of $p(\bar{\rho}_{i+\frac{1}{2},j+\frac{1}{2}})$ (which is similar to (11)). Indeed, bearing in mind the expansion (12) of a_d , we have $\bar{p}_{i+\frac{1}{2},j+\frac{1}{2}}^{(2)} - \bar{p}_{i-\frac{1}{2},j+\frac{1}{2}}^{(2)} = a_d^{(0)} (\bar{\rho}_{i+\frac{1}{2},j+\frac{1}{2}}^{(2)} - \bar{\rho}_{i-\frac{1}{2},j+\frac{1}{2}}^{(2)})$.

We now turn to give a simple expression of the fluxes $\mathcal{G}_{i+\frac{1}{2},j+\frac{1}{2}}^{u,x,(0)}$ and $\mathcal{G}_{i,j}^{u,y,(0)}$ in the case where $\alpha = \epsilon^2$. We first remark that in this case

$$\tilde{c}^{(0)}(\rho, \nu) = |\nu^{(0)}|.$$

Going back to the definition of \mathcal{F}^\pm we thus observe that

$$\mathcal{F}^{+, (0)}(\rho, \nu) = \rho^{(0)}[\nu^{(0)}]^+ \quad \text{and} \quad \mathcal{F}^{-, (0)}(\rho, \nu) = -\rho^{(0)}[\nu^{(0)}]^-.$$

Hence we get $\mathcal{G}^{u,x,(0)} = \rho^{(0)}G^{u,x}$ and $\mathcal{G}^{u,y,(0)} = \rho^{(0)}G^{u,y}$ with

$$G_{i+\frac{1}{2},j+\frac{1}{2}}^{u,x} = \{u^{(0)}\}_{i+\frac{1}{2},j+\frac{1}{2}}^x \cdot \{u^{(0)}\}_{i+\frac{1}{2},j+\frac{1}{2}}^x - \{[u^{(0)}]\}_{i+\frac{1}{2},j+\frac{1}{2}}^x \cdot \llbracket u^{(0)} \rrbracket_{i+\frac{1}{2},j+\frac{1}{2}}^x \quad (16)$$

and

$$G_{i,j}^{u,y} = \frac{\{\delta xv^{(0)}\}_{i,j}^x}{\delta x_i} \cdot \{u^{(0)}\}_{i,j}^y - \frac{\{[\delta xv^{(0)}]\}_{i,j}^x}{\delta x_i} \cdot \llbracket u^{(0)} \rrbracket_{i,j}^y, \quad (17)$$

where we have introduced the following notations for the average and the jump of a quantity Q , for k and l in \mathbb{N} or $\mathbb{N} + \frac{1}{2}$,

$$\begin{aligned} \{Q\}_{k,l}^x &= \frac{Q_{k-\frac{1}{2},l} + Q_{k+\frac{1}{2},l}}{2} & \text{and} & \quad \{Q\}_{k,l}^y = \frac{Q_{k,l-\frac{1}{2}} + Q_{k,l+\frac{1}{2}}}{2}, \\ \llbracket Q \rrbracket_{k,l}^x &= \frac{Q_{k+\frac{1}{2},l} - Q_{k-\frac{1}{2},l}}{2} & \text{and} & \quad \llbracket Q \rrbracket_{k,l}^y = \frac{Q_{k,l+\frac{1}{2}} - Q_{k,l-\frac{1}{2}}}{2}. \end{aligned}$$

The fluxes $G_{i+\frac{1}{2},j+\frac{1}{2}}^{u,x}$ (resp. $G_{i,j}^{u,y}$) can be interpreted as fluxes in the horizontal (resp. vertical) direction of the advected quantity $u^{(0)}$ at velocity $u^{(0)}$ (resp. $v^{(0)}$). We obtain a similar expression of the fluxes for the second component of the velocity v :

$$G_{i+\frac{1}{2},j+\frac{1}{2}}^{v,y} = \{v^{(0)}\}_{i+\frac{1}{2},j+\frac{1}{2}}^y \cdot \{v^{(0)}\}_{i+\frac{1}{2},j+\frac{1}{2}}^y - \{[v^{(0)}]\}_{i+\frac{1}{2},j+\frac{1}{2}}^y \cdot \llbracket v^{(0)} \rrbracket_{i+\frac{1}{2},j+\frac{1}{2}}^y \quad (18)$$

and

$$G_{i,j}^{v,x} = \frac{\{\delta yu^{(0)}\}_{i,j}^y}{\delta y_j} \cdot \{v^{(0)}\}_{i,j}^x - \frac{\{[\delta yu^{(0)}]\}_{i,j}^y}{\delta y_j} \cdot \llbracket v^{(0)} \rrbracket_{i,j}^x. \quad (19)$$

Thus, with similar calculation for the vertical component, we arrive at the following result

Proposition 2.10. *When setting $\alpha = \epsilon^2$, formally, as ϵ tends to zero, the compressible Euler solver (SDD)-(FDD) behaves like the following scheme for solving the Incompressible Euler system (3)*

$$\left\{ \begin{aligned} & \frac{\bar{u}_{i,j+\frac{1}{2}}^{(0)} - u_{i,j+\frac{1}{2}}^{(0)}}{\delta t} + \frac{G_{i+\frac{1}{2},j+\frac{1}{2}}^{u,x} - G_{i-\frac{1}{2},j+\frac{1}{2}}^{u,x}}{\delta x_i} + \frac{G_{i,j+1}^{u,y} - G_{i,j}^{u,y}}{\delta y_{j+\frac{1}{2}}} \\ & \quad + \frac{1}{\rho^{(0)}} \frac{\bar{p}_{i+\frac{1}{2},j+\frac{1}{2}}^{(2)} - \bar{p}_{i-\frac{1}{2},j+\frac{1}{2}}^{(2)}}{\delta x_i} = 0, \\ & \frac{\bar{v}_{i+\frac{1}{2},j}^{(0)} - v_{i+\frac{1}{2},j}^{(0)}}{\delta t} + \frac{G_{i+\frac{1}{2},j+\frac{1}{2}}^{v,y} - G_{i+\frac{1}{2},j-\frac{1}{2}}^{v,y}}{\delta y_j} + \frac{G_{i+1,j}^{v,x} - G_{i,j}^{v,x}}{\delta x_{i+\frac{1}{2}}} \\ & \quad + \frac{1}{\rho^{(0)}} \frac{\bar{p}_{i+\frac{1}{2},j+\frac{1}{2}}^{(2)} - \bar{p}_{i+\frac{1}{2},j-\frac{1}{2}}^{(2)}}{\delta y_j} = 0, \\ & \nabla \mathbf{d} \cdot \bar{\mathbf{u}}_{i+\frac{1}{2},j+\frac{1}{2}}^{(0)} = 0, \end{aligned} \right. \quad (20)$$

with the definitions (16), (17), (18), (19) for fluxes G .

Remark 2.11. The 1D version of the fluxes G for the linear transport equation with constant velocity is exactly the upwind fluxes. In the case of the 1D Burgers equation $\partial_t u + \partial_x \left(\frac{u^2}{2} \right) = 0$, the analogue of the fluxes G would be the following fluxes:

$$G_{i+\frac{1}{2}} = \frac{1}{4} \begin{cases} (u_i + u_{i+1})u_i & \text{if } u_i > 0 \text{ and } u_{i+1} > 0, \\ (u_i + u_{i+1})u_{i+1} & \text{if } u_i < 0 \text{ and } u_{i+1} < 0, \\ 2u_i u_{i+1} & \text{if } u_i < 0 < u_{i+1}, \\ u_{i+1}^2 + u_i^2 & \text{if } u_i > 0 > u_{i+1}. \end{cases}$$

Numerical experiments show that these fluxes do not produce non entropic shocks, in contrast to the upwind scheme which is known to be non entropic since it captures wrong stationary shock solutions [30, Sections 13 & 14].

In the limit scheme (20), the divergence free constraint on the velocity can also be written as an elliptic problem for the pressure which reads as follows:

$$\Delta_d \bar{p}_{i+\frac{1}{2},j+\frac{1}{2}}^{(2)} = -\rho^{(0)} \left(\frac{\mathcal{U}_{i+1,j+\frac{1}{2}} - \mathcal{U}_{i,j+\frac{1}{2}}}{\delta x_{i+\frac{1}{2}}} + \frac{\mathcal{V}_{i+\frac{1}{2},j+1} - \mathcal{V}_{i+\frac{1}{2},j}}{\delta y_{j+\frac{1}{2}}} \right), \quad (21)$$

where $\mathcal{U}_{i,j+\frac{1}{2}}$ and $\mathcal{V}_{i+\frac{1}{2},j}$ are defined by

$$\begin{aligned} \mathcal{U}_{i,j+\frac{1}{2}} &= \frac{G_{i+\frac{1}{2},j+\frac{1}{2}}^{u,x} - G_{i-\frac{1}{2},j+\frac{1}{2}}^{u,x}}{\delta x_i} + \frac{G_{i,j+1}^{u,y} - G_{i,j}^{u,y}}{\delta y_{j+\frac{1}{2}}}, \\ \mathcal{V}_{i+\frac{1}{2},j} &= \frac{G_{i+\frac{1}{2},j+\frac{1}{2}}^{v,y} - G_{i+\frac{1}{2},j-\frac{1}{2}}^{v,y}}{\delta y_j} + \frac{G_{i+1,j}^{v,x} - G_{i,j}^{v,x}}{\delta x_{i+\frac{1}{2}}}. \end{aligned}$$

Note that Δ_d is the standard 5–points discretization of the Laplace operator, in contrast to the operator that arises in the original scheme [20, eq. (28)] which decouples odd/even points of the discretization. This is a well-known drawback of colocalized methods which can lead to spurious oscillations due to the nontrivial checkerboard modes that belong to the kernel of the operator. Using staggered grids avoids this difficulty; it can be related to the MAC discretization, which gets rid of these spurious modes [12].

Note that, as mentioned in Remark 2.8, the limit scheme (written here only in the case $\alpha = \epsilon^2$) automatically projects the initial velocity to discrete-divergence-free velocity fields. Actually, for the first time step the elliptic problem (21) should be written

$$\Delta_d \bar{p}_{i+\frac{1}{2},j+\frac{1}{2}}^{(2)} = -\rho^{(0)} \left(\frac{\mathcal{U}_{i+1,j+\frac{1}{2}} - \mathcal{U}_{i,j+\frac{1}{2}}}{\delta x_{i+\frac{1}{2}}} + \frac{\mathcal{V}_{i+\frac{1}{2},j+1} - \mathcal{V}_{i+\frac{1}{2},j}}{\delta y_{j+\frac{1}{2}}} \right) + \frac{\nabla_d \cdot \mathbf{u}_{i+\frac{1}{2},j+\frac{1}{2}}^{(0)}}{\delta t},$$

which enforces $\nabla_d \cdot \bar{\mathbf{u}}^{(0)} = 0$ as required in the limit scheme (20) even if $\nabla_d \cdot \mathbf{u}^{(0)} \neq 0$.

3 Numerical simulations

In this section we present some numerical test cases, in 1D and 2D, to illustrate the performances of the proposed scheme. In particular, we point out in the numerical experiments the stability and consistency issues.

As suggested above, we use $\alpha = \epsilon^2$ for all numerical experiments and otherwise specified, we adopt in the numerical tests the definition (9) with $\iota = 0$.

3.1 Simulation of 1D Riemann problems in low Mach regime

We start with a simple 1D Riemann problem, issued from [14]. The solution is made of two moving rarefaction waves, a left and a right one, separated by a constant state. The pressure law is given by $p(\rho) = \rho^2$ and the initial conditions are

$$\rho^{(0)}(x) = \begin{cases} 1 + \epsilon^2 & \text{if } x < 0.5, \\ 1 & \text{if } x > 0.5, \end{cases} \quad \text{and} \quad u^{(0)}(x) = \begin{cases} 1 - \epsilon & \text{if } x < 0.5, \\ 1 + \epsilon & \text{if } x > 0.5. \end{cases}$$

We compute the solution on the interval $(0, 1)$ for three different values of (ϵ, T) where T is the final time. For each case, the number of grid points is $N = 200$ and the time step is defined by $\delta t = \beta \delta x$ with $\beta = 0.2, 0.1$ or 0.01 . We compare the results produced by the AP scheme described in this paper with the results given by the first order explicit scheme of [3].

We first choose ϵ close to one ($\epsilon = \sqrt{0.99}$) and thus the Fast Dynamics part of the scheme does not play a significant role in the resolution. The results obtained with the two schemes are very close and all the values of β can be used. The results obtained with $\beta = 0.2$ at time $T = 0.1$ are reported in Figure 2.

We then choose ϵ smaller ($\epsilon = \sqrt{0.1}$) and for $\beta = 0.2$ the fully explicit scheme returns a negative density (which means that the CFL condition for this scheme is violated and the time step should be reduced) whereas the AP scheme still returns a relevant result. A time step divided by 2 (that is $\beta = 0.1$) ensures the positivity of the density for both schemes. The results obtained with $\beta = 0.2$ (for the AP scheme) and $\beta = 0.1$ at time $T = 0.05$ are reported in Figure 3.

Finally we choose ϵ close to zero ($\epsilon = \sqrt{0.001}$) and the explicit scheme returns a negative density for $\beta = 0.2$ and $\beta = 0.1$. We recover a relevant result with $\beta = 0.01$. The AP scheme provides a relevant results for all the values of β . The results obtained with $\beta = 0.2, 0.1$ (for the AP scheme) and $\beta = 0.01$ at time $T = 0.007$ are reported in Figure 4.

This test confirms that the stability condition for the explicit method is sensitive to the value of the Mach number ϵ and it shows that the AP strategy allows us to keep significantly larger time steps. It leads to significant computational cost savings (especially when $\epsilon \ll 1$), but obviously at the price of a loss of accuracy.

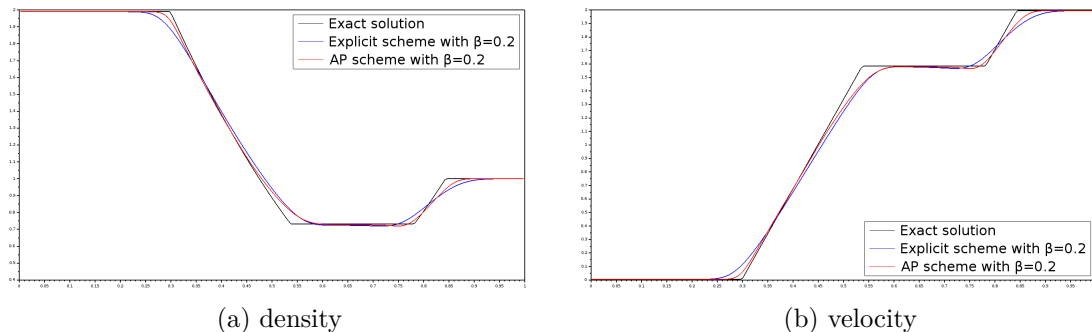


Figure 2: 1D Riemann problem, comparison between the AP scheme and an explicit scheme for $(\epsilon, T) = (\sqrt{0.99}, 0.1)$ and $\delta t = \beta \delta x$.

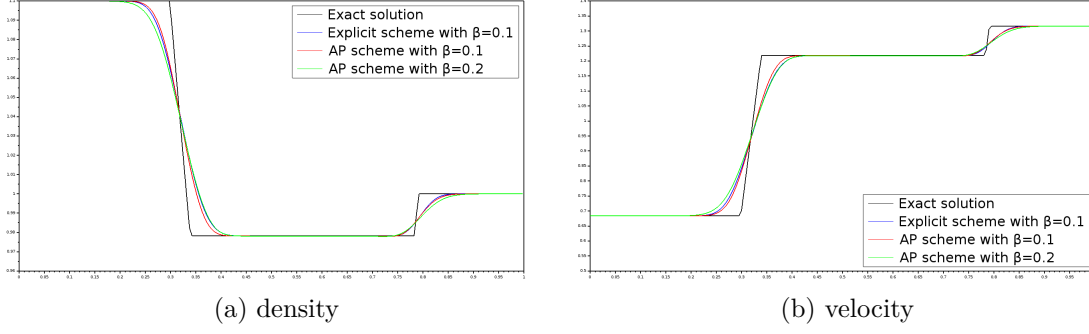


Figure 3: 1D Riemann problem, comparison between the AP scheme and an explicit scheme for $(\epsilon, T) = (\sqrt{0.1}, 0.05)$ and $\delta t = \beta \delta x$.

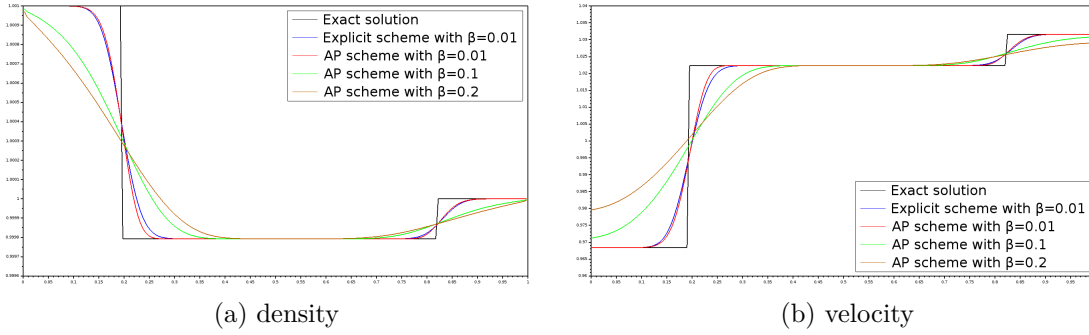


Figure 4: 1D Riemann problem, comparison between the AP scheme and an explicit scheme for $(\epsilon, T) = (\sqrt{0.001}, 0.007)$ and $\delta t = \beta \delta x$.

3.2 Low Mach regime simulations in 2D

We discuss several test cases in 2D, all with periodic boundary conditions. We adopt the following notation. For discrete quantities ρ , u or v , depending on their location, we introduce the L^1 and L^∞ discrete norms

$$\begin{aligned} \|\rho\|_1 &= \sum_{i,j} \delta x_{i+1/2} \delta y_{j+1/2} |\rho_{i+1/2,j+1/2}|, & \|\rho\|_\infty &= \max_{i,j} |\rho_{i+1/2,j+1/2}|, \\ \|u\|_1 &= \sum_{i,j} \delta x_i \delta y_{j+1/2} |u_{i,j+1/2}|, & \|u\|_\infty &= \max_{i,j} |u_{i,j+1/2}|, \\ \|v\|_1 &= \sum_{i,j} \delta x_{i+1/2} \delta y_j |v_{i+1/2,j}|, & \|v\|_\infty &= \max_{i,j} |v_{i+1/2,j}|. \end{aligned}$$

To evaluate the behaviour of the scheme when the mesh size goes to zero, associated to a quantity q (which can stand for ρ , u or v), we consider the following errors in L^1 or L^∞ discrete norm

$$e_{1,q}^{(N)} = \|q^{(N)} - q^{\text{exact}}\|_1 \quad \text{and} \quad e_{\infty,q}^{(N)} = \|q^{(N)} - q^{\text{exact}}\|_\infty,$$

where $q^{(N)}$ stands for the approximate solution obtained on a $N \times N$ grid, whereas q^{exact} is the exact solution. Similarly, to evaluate the behaviour of the scheme when ϵ goes to zero, we introduce the following quantities

$$\mathbf{e}_{1,q}^{(\epsilon)} = \|q^{(\epsilon)} - q^{(0)}\|_1 \quad \text{and} \quad \mathbf{e}_{\infty,q}^{(\epsilon)} = \|q^{(\epsilon)} - q^{(0)}\|_\infty,$$

where $q^{(\epsilon)}$ stands for the approximate solution obtained for a fixed value of ϵ , whereas $q^{(0)}$ is the exact solution of the limit problem when $\epsilon \rightarrow 0$. In the computation of the norms, the expression of q^{exact} and $q^{(0)}$ are simply evaluated at the corresponding grid points.

3.2.1 Test 1: traveling vortex

The traveling vortex test case is extracted from [26]. The exact solution is known and a direct comparison is possible. We consider the domain $[0, 1] \times [0, 1]$. The pressure law is given by $p(\rho) = \frac{1}{2}\rho^2$ and the initial density and velocity are given by

$$\begin{aligned}\rho(x, y, 0) &= 110 + \frac{\epsilon^2}{(4\pi)^2} f(r_c), \\ \mathbf{u}(x, y, 0) &= \begin{pmatrix} v_0 \\ v_1 \end{pmatrix} + g(r_c) \begin{pmatrix} 0.5 - y \\ x - 0.5 \end{pmatrix},\end{aligned}$$

where $r_c = 4\pi((x - 0.5)^2 + (y - 0.5)^2)^{\frac{1}{2}}$ and f, g are two functions such that f is continuous and piecewise \mathcal{C}^1 , g is continuous and

$$f'(r) = rg(r)^2, \quad \text{for almost all } r.$$

This problem reduces to a pure transport, the vortex is traveling at speed (v_0, v_1) : the exact solution is simply

$$\begin{aligned}\rho(x, y, t) &= \rho(x - v_0 t, y - v_1 t, 0), \\ \mathbf{u}(x, y, t) &= \mathbf{u}(x - v_0 t, y - v_1 t, 0).\end{aligned}$$

As in [26], we first choose

$$\begin{aligned}f(r) &= (1.5)^2 \delta(r_c) (k(r_c) - k(\pi)), \\ g(r) &= 1.5(1 + \cos(r_c)) \delta(r_c), \\ v_0 &= 0.6, \quad v_1 = 0,\end{aligned}$$

where

$$\begin{aligned}k(r) &= 2 \cos(r) + 2r \sin(r) + \frac{1}{8} \cos(2r) + \frac{1}{4} r \sin(2r) + \frac{3}{4} r^2, \\ \delta(r) &= \mathbb{1}_{r < \pi}.\end{aligned}$$

We observe in numerical simulations for this test case some spurious oscillations for large values of ϵ (for instance $\epsilon = 0.8$ and $\epsilon = 0.5$) when we set $\iota = 0$ in the definition (9) of the coefficient a_d . We observe that setting $\iota = 1$ is sufficient to eliminate these oscillations so that we adopt this definition for all the simulations performed for this test case. In Figures 5, 6 and 7 we show the density, the horizontal and vertical velocity respectively at initial time (left) and final time $T = 0.5$ (right) for $\epsilon = 0.8$, $\delta x = \delta y = 1/32$ and $\delta t = 5 \times 10^{-4}$. Cuts are available in Figure 8. Numerical solutions at time $T = 0$ (blue solid lines) and $T = 0.5$ (black dashed lines) are represented. The density (top) and the vertical velocity (bottom right) are plotted along the line $y = 0.5$ as a function of $x - v_0 T$. It allows us to compare the shape of the initial solution and the shape of the numerical solution at time $T = 0.5$. The horizontal velocity (bottom left) is plotted along the line $x = 0.5 + v_0 T$ as a function of y . The results are oscillations-free but we observe an important numerical diffusion inherent to the use of a first order scheme.

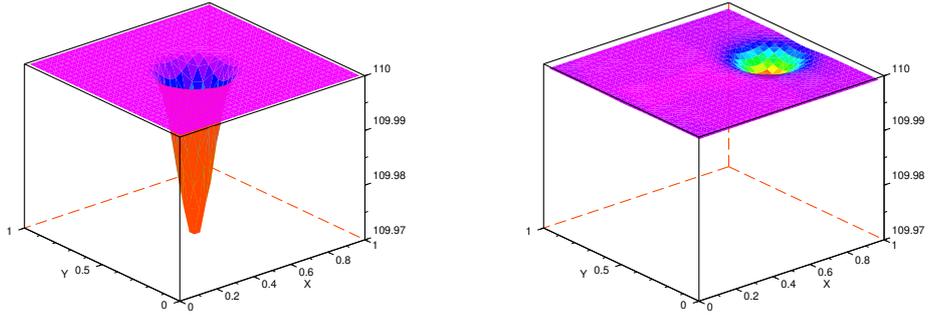


Figure 5: Test 1 (traveling vortex), density at time $T = 0$ (left) and $T = 0.5$ (right). At $T = 0.5$, $\min_{i,j} \rho_{i+\frac{1}{2},j+\frac{1}{2}} = 109.9951$.

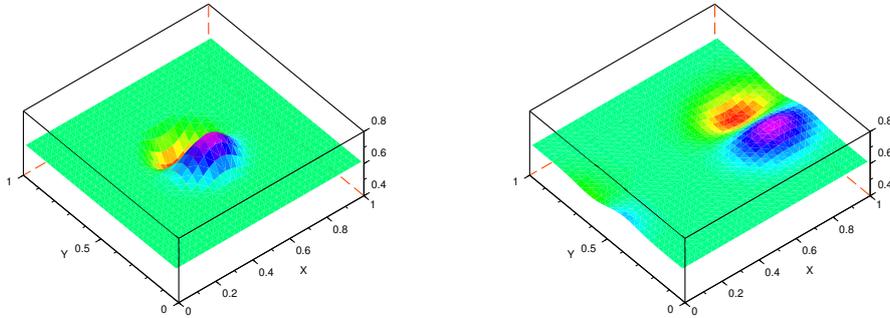


Figure 6: Test 1 (traveling vortex), horizontal velocity at time $T = 0$ (left) and $T = 0.5$ (right). At $T = 0.5$, $\min_{i,j} u_{i,j+\frac{1}{2}} = 0.52$, $\max_{i,j} u_{i,j+\frac{1}{2}} = 0.67$.

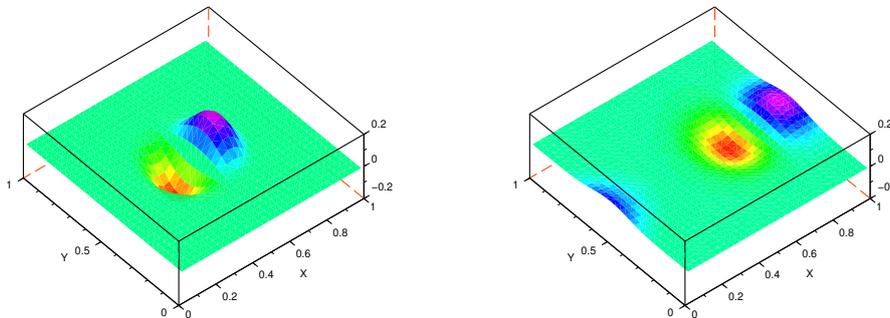


Figure 7: Test 1 (traveling vortex), vertical velocity at time $T = 0$ (left) and $T = 0.5$ (right). At $T = 0.5$, $\min_{i,j} v_{i+\frac{1}{2},j} = -0.069$, $\max_{i,j} v_{i+\frac{1}{2},j} = 0.064$.

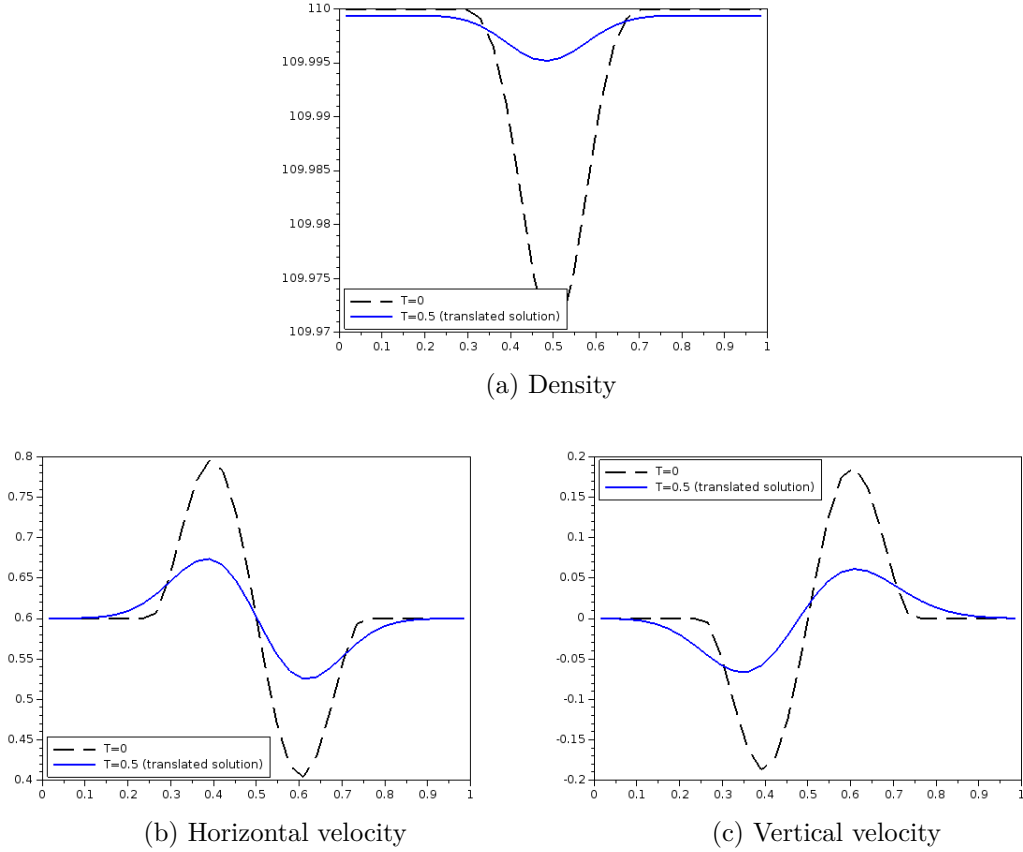


Figure 8: Test 1 (traveling vortex), translated cuts at time $T = 0$ (blue solid lines) and $T = 0.5$ (black dashed lines). Density along $y = 0.5$ as a function of $x - v_0T$ (top). Horizontal velocity along $x = 0.5 + v_0T$ as a function of y (bottom left). Vertical velocity along $y = 0.5$ as a function of $x - v_0T$ (bottom right).

We then provide a convergence study in Fig 9. For different Mach numbers $\epsilon \in \{0.01, 0.1, 0.4, 0.8\}$, we perform computations with $\delta t = 5 \times 10^{-4}$ on different grids (10×10 , 14×14 , 20×20 , 28×28 , 40×40 and 56×56). We plot in logarithmic scales the discrete L^1 error norm at time $T = 0.01$ between the exact solution and the discrete one (for the density on the left and for the first component of the velocity on the right) as a function of the mesh size. We clearly observe a first order convergence. Similar results are obtained for the second component of the velocity.

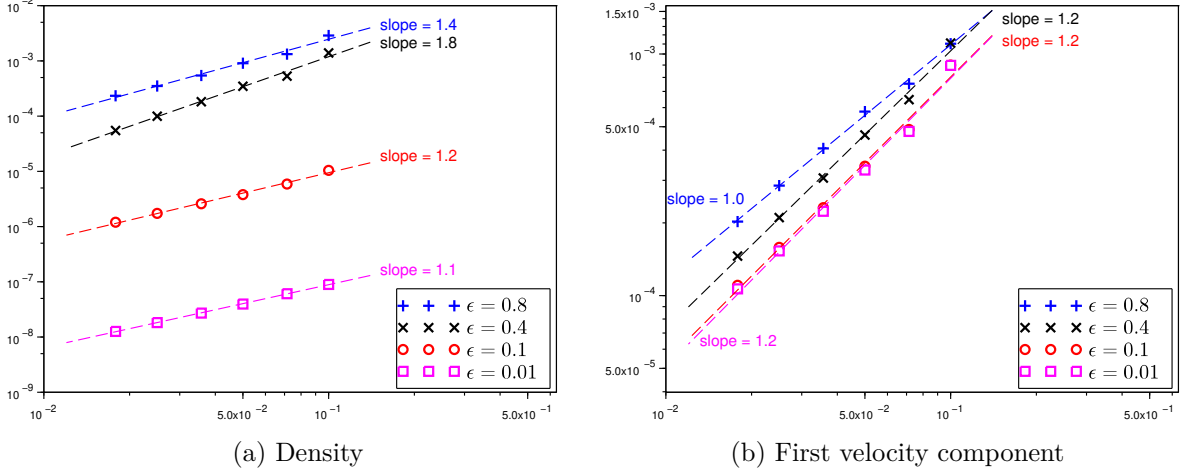


Figure 9: Test 1 (traveling vortex) L^1 error norm at $T = 0.01$ as a function of the mesh size for different values of ϵ and $\delta t = 5 \times 10^{-4}$.

Finally, to justify the AP character of the scheme, using a 32×32 grid and a time step $\delta t = 5 \times 10^{-4}$, we study for different values of the Mach number $\epsilon \in \{0.0125, 0.025, 0.05, 0.1, 0.2, 0.4, 0.8\}$, the discrete L^1 and L^∞ -norm at time $T = 0.01$ of the difference between the discrete solution and $\rho^{(0)} = 110$. The results are reported in Table 1. It confirms that the density tends to be constant, equal to $\rho^{(0)}$ when ϵ tends to zero and that the norm of the difference behaves like $c\epsilon^2$ (with c a constant independent of ϵ).

ℓ	ϵ_ℓ	$\mathbf{e}_{1,\rho}^{(\epsilon_\ell)}$	$\frac{\log(\mathbf{e}_{1,\rho}^{(\epsilon_{\ell+1})}/\mathbf{e}_{1,\rho}^{(\epsilon_\ell)})}{\log(\epsilon_{\ell+1}/\epsilon_\ell)}$	$\mathbf{e}_{\infty,\rho}^{(\epsilon_\ell)}$	$\frac{\log(\mathbf{e}_{\infty,\rho}^{(\epsilon_{\ell+1})}/\mathbf{e}_{\infty,\rho}^{(\epsilon_\ell)})}{\log(\epsilon_{\ell+1}/\epsilon_\ell)}$
1	0.8	1.06×10^{-3}	1.62	2.54×10^{-2}	1.84
2	0.4	3.44×10^{-4}	2.24	7.11×10^{-3}	2.00
3	0.2	7.30×10^{-5}	2.32	1.78×10^{-3}	2.00
4	0.1	1.46×10^{-5}	2.00	4.46×10^{-4}	1.99
5	0.05	3.64×10^{-6}	2.00	1.12×10^{-4}	2.01
6	0.025	9.13×10^{-7}	2.00	2.79×10^{-5}	2.00
7	0.0125	2.28×10^{-7}	--	6.97×10^{-6}	--

Table 1: Test 1 (traveling vortex) Errors $\mathbf{e}_{1,\rho}^{(\epsilon_\ell)} = \|\rho^{(\epsilon_\ell)} - \rho^{(0)}\|_1$ and $\mathbf{e}_{\infty,\rho}^{(\epsilon_\ell)} = \|\rho^{(\epsilon_\ell)} - \rho^{(0)}\|_\infty$ at $T = 0.01$ for different ϵ on a 32×32 grid and $\delta t = 5 \times 10^{-4}$.

Next, concerning the velocity, we provide in Table 2, for different values of $\epsilon \in \{0.0125, 0.025, 0.05, 0.1, 0.2, 0.4, 0.8\}$ and at $T = 0.01$, the L^1 norm of the discrete divergence and the L^1 norm of the difference between the approximate velocity $u^{(\epsilon)}$ and the exact limit velocity $u^{(0)}$ obtained when $\epsilon \rightarrow 0$. Unfortunately, this test case does not illustrate the fact that the approximate velocity converges towards the correct solution when $\epsilon \rightarrow 0$. Indeed, in Table 2, the difference in L^1 norm seems to remain close to 2×10^{-4} when ϵ goes to 0. This is probably due to the fact that, in this test case, contrarily to the density, the exact velocity does not depend on ϵ or, in other words, this is due to the fact that, even for $\epsilon \neq 0$, the exact velocity is equal to the limit velocity. Therefore, the observed difference is certainly a truncation error

due to the mesh rather than a difference due to a positive value of ϵ . Nevertheless, even if this difference does not vanish when $\epsilon \rightarrow 0$, we observe that the discrete divergence goes to 0, in accordance with Remark 2.8. For small values of ϵ , we recover that the norm of the discrete divergence behaves like $c\epsilon^2$ as expected.

ℓ	ϵ_ℓ	$\mathbf{e}_{1,\text{div}}^{(\epsilon_\ell)}$	$\frac{\log(\mathbf{e}_{1,\text{div}}^{(\epsilon_{\ell+1})}/\mathbf{e}_{1,\text{div}}^{(\epsilon_\ell)})}{\log(\epsilon_{\ell+1}/\epsilon_\ell)}$	$\mathbf{e}_{1,u}^{(\epsilon_\ell)}$
1	0.8	1.37×10^{-3}	1.15	3.60×10^{-4}
2	0.4	6.16×10^{-4}	1.92	2.69×10^{-4}
3	0.2	1.63×10^{-4}	4.21	2.15×10^{-4}
4	0.1	8.81×10^{-6}	5.90	2.03×10^{-4}
5	0.05	1.48×10^{-7}	1.96	1.98×10^{-4}
6	0.025	3.80×10^{-8}	1.95	1.97×10^{-4}
7	0.0125	9.82×10^{-9}	--	1.96×10^{-4}

Table 2: Test 1 (traveling vortex) Discrete L^1 norm of the discrete divergence $\mathbf{e}_{1,\text{div}}^{(\epsilon_\ell)} = \|\nabla_d \cdot \mathbf{u}^{(\epsilon_\ell)}\|_1$ and error $\mathbf{e}_{1,u}^{(\epsilon_\ell)} = \|u^{(\epsilon_\ell)} - u^{(0)}\|_1$ at $T = 0.01$ for different ϵ on a 32×32 grid and $\delta t = 5 \times 10^{-4}$.

In Table 3, we present the results of the same study on a finer mesh (a 64×64 grid). The behaviour of the discrete divergence is similar and, as previously, we also observe that the difference in L^1 norm between the approximate velocity $u^{(\epsilon)}$ and the exact limit velocity $u^{(0)}$ does not vanish. However it now remains close to 9.30×10^{-5} . It confirms the hypothesis that this almost constant error could be due to the discretization error since it becomes (approximatively) twice smaller on a twice finer grid.

ℓ	ϵ_ℓ	$\mathbf{e}_{1,\text{div}}^{(\epsilon_\ell)}$	$\frac{\log(\mathbf{e}_{1,\text{div}}^{(\epsilon_{\ell+1})}/\mathbf{e}_{1,\text{div}}^{(\epsilon_\ell)})}{\log(\epsilon_{\ell+1}/\epsilon_\ell)}$	$\mathbf{e}_{1,u}^{(\epsilon_\ell)}$
1	0.8	9.98×10^{-4}	2.49	1.77×10^{-4}
2	0.4	1.78×10^{-4}	2.15	1.27×10^{-4}
3	0.2	4.00×10^{-5}	4.18	1.03×10^{-4}
4	0.1	2.20×10^{-6}	4.77	9.62×10^{-5}
5	0.05	8.04×10^{-8}	1.99	9.40×10^{-5}
6	0.025	2.02×10^{-8}	1.97	9.33×10^{-5}
7	0.0125	5.15×10^{-9}	--	9.31×10^{-5}

Table 3: Test 1 (traveling vortex) Discrete L^1 norm of the discrete divergence $\mathbf{e}_{1,\text{div}}^{(\epsilon_\ell)} = \|\nabla_d \cdot \mathbf{u}^{(\epsilon_\ell)}\|_1$ and error $\mathbf{e}_{1,u}^{(\epsilon_\ell)} = \|u^{(\epsilon_\ell)} - u^{(0)}\|_1$ at $T = 0.01$ for several ϵ on a 64×64 grid and $\delta t = 5 \times 10^{-4}$.

To observe the behaviour of the discrete velocity when ϵ goes to zero, we propose to study

a perturbed version of this test case, more relevant for our purpose, by setting

$$\begin{aligned} f(r) &= (1.5 + \epsilon)^2 \delta(r_c)(k(r_c) - k(\pi)), \\ g(r) &= (1.5 + \epsilon)(1 + \cos(r_c))\delta(r_c). \end{aligned}$$

The results are reported in Table 4 (for the density) and in Table 5 (for the velocity and the divergence of the velocity). The behaviour of $\rho^{(\epsilon)}$ and $\nabla_{\mathbf{d}} \cdot \mathbf{u}^{(\epsilon)}$ remains unchanged. But we now clearly observe that the discrete velocity tends to the exact limit velocity when ϵ tends to zero and, as expected, that the norm of the difference behaves like $c\epsilon$ (with c a constant independent of ϵ).

ℓ	ϵ_ℓ	$\mathbf{e}_{1,\rho}^{(\epsilon_\ell)}$	$\frac{\log(\mathbf{e}_{1,\rho}^{(\epsilon_{\ell+1})}/\mathbf{e}_{1,\rho}^{(\epsilon_\ell)})}{\log(\epsilon_{\ell+1}/\epsilon_\ell)}$
1	0.8	2.34×10^{-3}	2.20
2	0.4	5.10×10^{-4}	2.48
3	0.2	9.12×10^{-5}	2.46
4	0.1	1.66×10^{-5}	2.09
5	0.05	3.89×10^{-6}	2.04
6	0.025	9.44×10^{-7}	2.02
7	0.0125	2.32×10^{-7}	--

Table 4: Test 1 (traveling vortex, perturbed version) Discrete L^1 norm of $\mathbf{e}_{1,\rho}^{(\epsilon_\ell)} = \|\rho^{(\epsilon_\ell)} - \rho^{(0)}\|_1$ at $T = 0.01$ for different ϵ on a 32×32 grid and $\delta t = 5 \times 10^{-4}$.

ℓ	ϵ_ℓ	$\mathbf{e}_{1,\text{div}}^{(\epsilon_\ell)}$	$\frac{\log(\mathbf{e}_{1,\text{div}}^{(\epsilon_{\ell+1})}/\mathbf{e}_{1,\text{div}}^{(\epsilon_\ell)})}{\log(\epsilon_{\ell+1}/\epsilon_\ell)}$	$\mathbf{e}_{1,u}^{(\epsilon_\ell)}$	$\frac{\log(\mathbf{e}_{1,u}^{(\epsilon_{\ell+1})}/\mathbf{e}_{1,u}^{(\epsilon_\ell)})}{\log(\epsilon_{\ell+1}/\epsilon_\ell)}$
1	0.8	2.81×10^{-3}	1.82	6.45×10^{-3}	0.98
2	0.4	7.98×10^{-4}	2.10	3.26×10^{-3}	1.01
3	0.2	1.86×10^{-4}	4.30	1.62×10^{-3}	0.99
4	0.1	9.43×10^{-6}	5.90	8.13×10^{-4}	1.00
5	0.05	1.58×10^{-7}	2.01	4.06×10^{-4}	0.98
6	0.025	3.93×10^{-8}	1.98	2.06×10^{-4}	0.52
7	0.0125	9.99×10^{-9}	2.00	1.44×10^{-4}	--

Table 5: Test 1 (traveling vortex, perturbed version) Discrete L^1 norm of the discrete divergence $\mathbf{e}_{1,\text{div}}^{(\epsilon_\ell)} = \|\nabla_{\mathbf{d}} \cdot \mathbf{u}^{(\epsilon_\ell)}\|_1$ and $\mathbf{e}_{1,u}^{(\epsilon_\ell)} = \|u^{(\epsilon_\ell)} - u^{(0)}\|_1$ at $T = 0.01$ for different ϵ on a 32×32 grid and $\delta t = 5 \times 10^{-4}$.

3.2.2 Test 2: cylindrical explosion problem

We consider a 2D isentropic cylindrical explosion problem extracted from [14]. The computational domain is $\Omega = [-1, 1] \times [-1, 1]$, discretized with a 50×50 grid. The pressure is given by

$p(\rho) = \rho$ and the initial density and velocity are given by

$$\begin{aligned}\rho(x, y, 0) &= 1 + \epsilon^2 \mathbb{1}_{r(x,y) \leq 1/4}, \\ u(x, y, 0) &= \frac{-x\beta(x, y)}{r(x, y)\rho(x, y, 0)} \mathbb{1}_{r(x,y) > 10^{-15}}, \\ v(x, y, 0) &= \frac{-y\beta(x, y)}{r(x, y)\rho(x, y, 0)} \mathbb{1}_{r(x,y) > 10^{-15}},\end{aligned}$$

where r is the distance to the center of the domain, $r(x, y) = \sqrt{x^2 + y^2}$ and

$$\beta(x, y) = \max\{0, 1 - r(x, y)\} \times \left(1 - e^{-16r(x,y)^2}\right).$$

The initial density and velocity field are shown in Fig. 10.

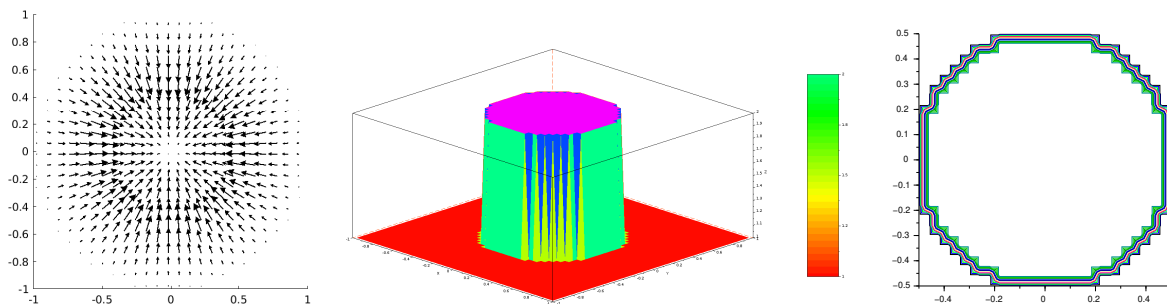


Figure 10: Test 2 (explosion problem), time $t = 0$ and $\epsilon = 1$, velocity field (left) and density profile (middle and right).

Like in [14] we display the numerical solution obtained at time $t = 0.1$, $t = 0.25$ and $t = 0.5$ for $\epsilon = 1$ in Fig. 11 to Fig. 13. The simulation is performed on a 50×50 grid with a time step $\delta t = 5 \times 10^{-4}$.

The results obtained for $\epsilon = 1$ at time $t = 0.1$ and $t = 0.5$ are very close to the results obtained with a different AP-scheme in [14]. Note that, as confirmed by its authors, the result reported in [14] for $t = 0.25$ does not correspond to this simulation time. We warmly thanks the authors for taking the time to re-consider this test case and for many useful hints.

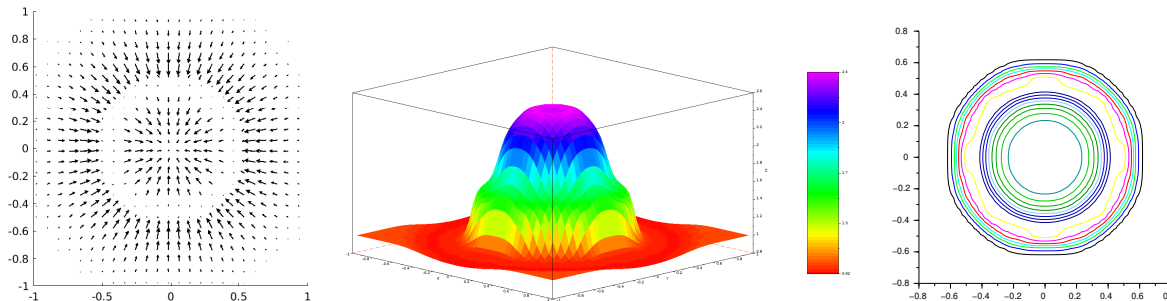


Figure 11: Test 2 (explosion problem), time $t = 0.1$ and $\epsilon = 1$, velocity field (left) and density profile (middle and right).

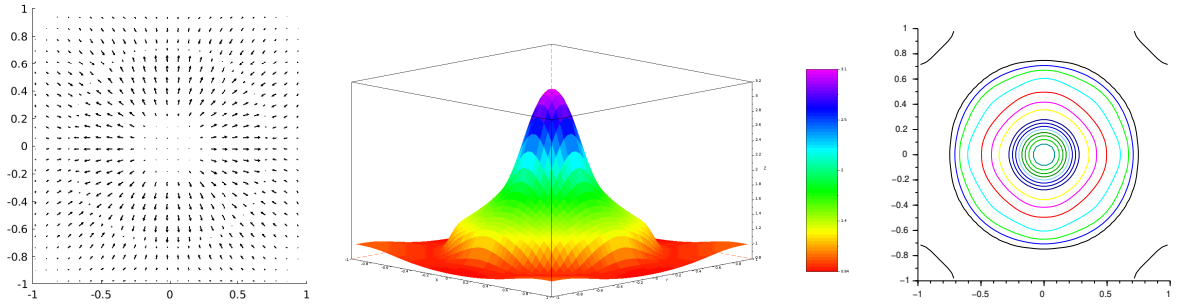


Figure 12: Test 2 (explosion problem), time $t = 0.25$ and $\epsilon = 1$, velocity field (left) and density profile (middle and right).

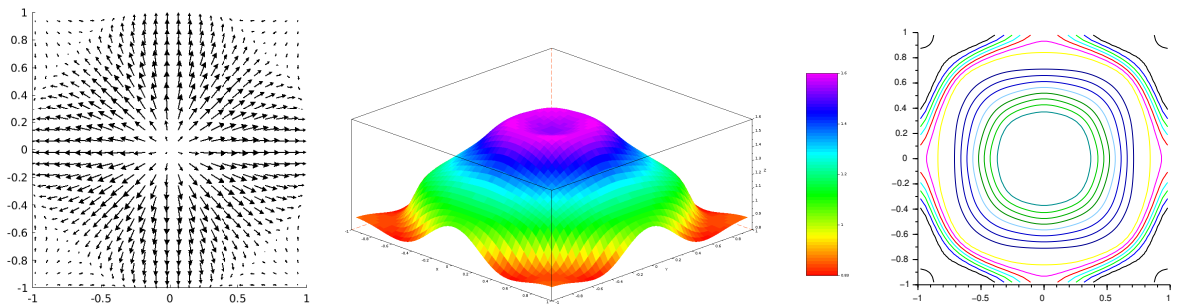


Figure 13: Test 2 (explosion problem), time $t = 0.5$ and $\epsilon = 1$, velocity field (left) and density profile (middle and right).

We present in Fig. 14 the results obtained at $t = 0.05$ using the AP-scheme with $\epsilon = 5 \times 10^{-3}$. We use again a 50×50 grid and compare the velocity fields obtained with a small time step, $\delta t = 10^{-4}$, at left and a large one, $\delta t = 5 \times 10^{-3}$, at right. As in [14], we observe that the AP scheme resolves the small waves dynamics when using a small time step but also that the AP-scheme can handle large time step and, in this case, it captures the limit solution.

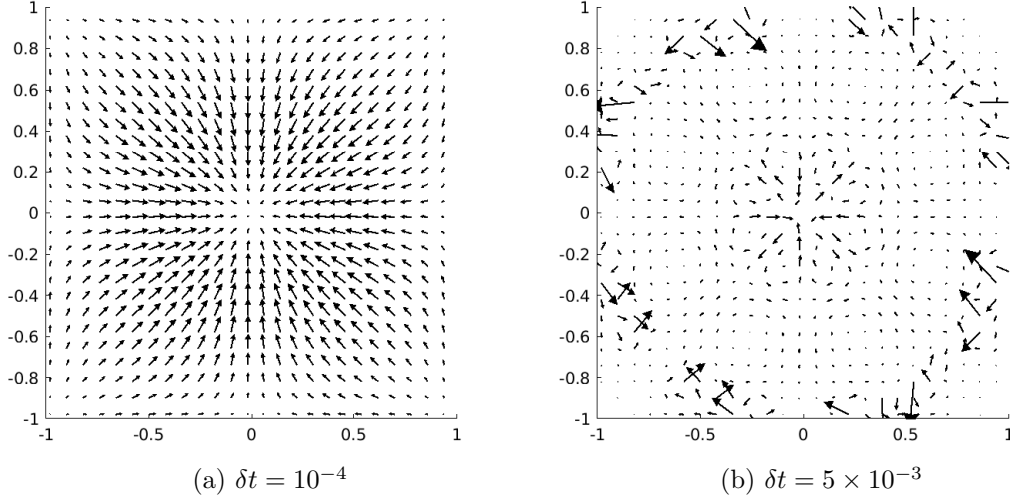


Figure 14: Test 2 (explosion problem), velocity field at time $t = 0.05$, using the AP-scheme with $\epsilon = 5 \times 10^{-3}$, comparison between the results obtained for $\delta t = 10^{-4}$ (left) and $\delta t = 5 \times 10^{-3}$ (right).

3.2.3 Test 3

The third test case is extracted from [8]. The computational domain is $\Omega = [0, 1] \times [0, 1]$. The final time is $T = 1$ and the time step is given by $\delta t = 2.5 \times 10^{-2}$. The pressure law is given by $p(\rho) = \rho^2$ and the initial data reads

$$\begin{aligned} \rho &= 1 + \epsilon^2 \sin^2(2\pi(x + y)), \\ q_u &= \sin(2\pi(x - y)) + \epsilon^2 \sin(2\pi(x + y)) \quad \text{and} \quad u = \frac{q_u}{\rho}, \\ q_v &= \sin(2\pi(x - y)) + \epsilon^2 \cos(2\pi(x + y)) \quad \text{and} \quad v = \frac{q_v}{\rho}. \end{aligned}$$

As in [8], we compute the solution for $\epsilon = 0.8$ and $\epsilon = 0.05$. For $\epsilon = 0.8$, the result in [8] is presented on a 20×20 grid; we obtain a similar figure with a 12×12 grid, but the results are different when the mesh is refined. With a 20×20 grid, the result given by the AP method is close to the one obtained with a 64×64 grid. Results for $\epsilon = 0.8$ using a 64×64 grid are presented in Figure 15. The result obtained with $\epsilon = 0.05$ using a 64×64 grid are presented in Figure 16 for the AP-Scheme and in Figure 17 with the limit scheme (20). The density obtained with the AP-scheme is almost equal to the constant state $\rho^{(0)} = 1$: $\|\rho - \rho^{(0)}\|_\infty \sim 10^{-3}$, the horizontal and vertical velocities have converged to the solution of the limit scheme.

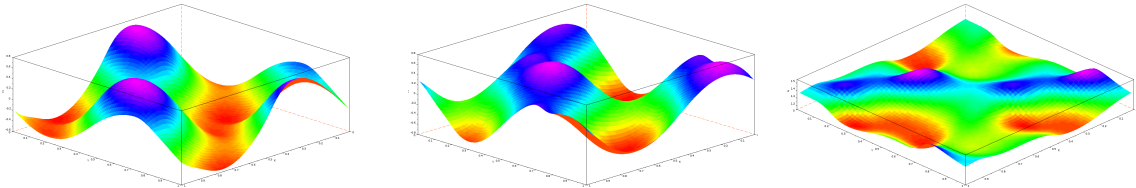


Figure 15: Test 3, $\epsilon = 0.8$, horizontal and vertical velocity (left and middle) and density (right).

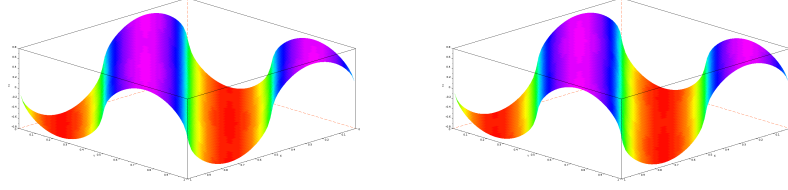


Figure 16: Test 3, $\epsilon = 0.05$, horizontal (left) and vertical velocity (right).

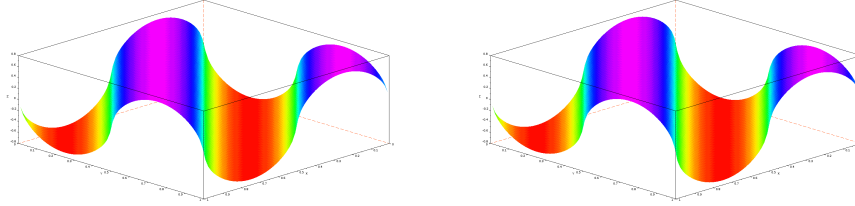


Figure 17: Test 3, horizontal (left) and vertical velocity (right) using the limit scheme (20).

3.3 Incompressible Euler simulations using the limit scheme

We now turn to the resolution of the incompressible Euler system in order to check the validity of the limit scheme (20). We consider two test cases from [15]. The computational domain is $\Omega = [0, 2\pi] \times [0, 2\pi]$ for both test cases. The density is assumed to be constant equal to 1.

3.3.1 Test A: analytical solution

We test the capability of the limit scheme (20) to (approximately) preserve a stationary solution of the incompressible Euler system:

$$u(x, y, t) = -\sin(x) \cos(y), \quad v(x, y, t) = \cos(x) \sin(y) \quad \text{and} \quad p(x, y, t) = \frac{1}{2}(\cos(x)^2 + \cos(y)^2).$$

The exact vorticity equal to

$$w(x, y, t) = -2 \sin(x) \sin(y).$$

The initial data is chosen as the evaluation on the grid of the stationary solution and using the limit scheme (20), we perform different numerical simulations up to time $T = 2$ on different meshes with a time step $\delta t = 2 \times 10^{-4}$.

The result obtained using a 160×160 mesh is reported in Figure 18 (vorticity) and in Figure 19 (velocity and pressure), the discrete vorticity w being defined by

$$w_{i,j} = \frac{v_{i+\frac{1}{2},j} - v_{i-\frac{1}{2},j}}{\delta x_i} - \frac{u_{i,j+\frac{1}{2}} - u_{i,j-\frac{1}{2}}}{\delta y_j}.$$

We next provide in Table 6 the L^∞ error norms $e_{\infty,u}^{(N)}$ and $e_{\infty,w}^{(N)}$, $N \in \{40, 60, 80, 100, 120, 140, 160\}$, for the horizontal velocity u (the results for the vertical velocity v are similar) and for the vorticity w . As expected, we observe a first order convergence.

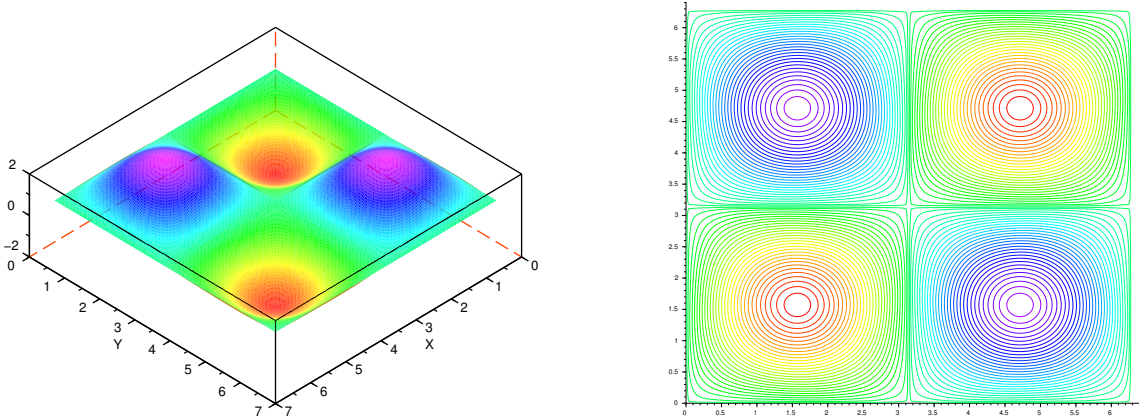


Figure 18: Test A, vorticity w using the limit scheme (20) at $T = 2$ on a 160×160 grid with $\delta t = 2 \times 10^{-4}$.

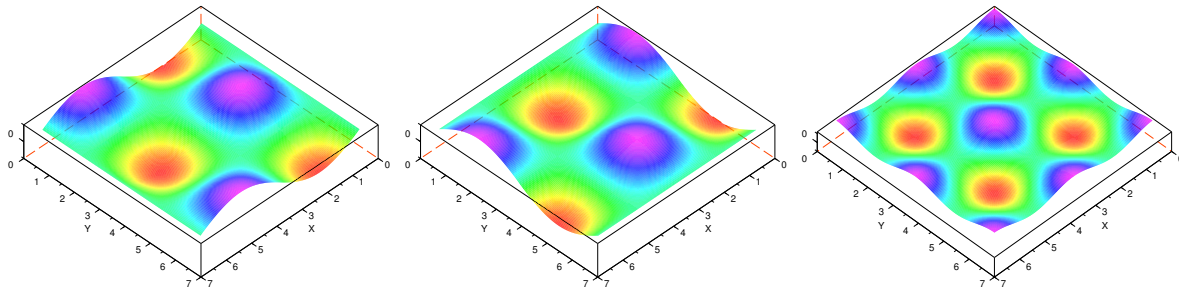


Figure 19: Test A, horizontal (left) and vertical (middle) velocity and pressure (right) using the limit scheme (20) at $T = 2$ on a 160×160 grid with $\delta t = 2 \times 10^{-4}$.

ℓ	N_ℓ	$e_{\infty,u}^{(N_\ell)}$	$\frac{\log(e_{1,u}^{(N_{\ell+1})}/e_{1,u}^{(N_\ell)})}{\log(N_\ell/N_{\ell+1})}$	$e_{\infty,w}^{(N_\ell)}$	$\frac{\log(e_{1,w}^{(N_{\ell+1})}/e_{1,w}^{(N_\ell)})}{\log(N_\ell/N_{\ell+1})}$
1	40	1.08×10^{-1}	0.85	2.58×10^{-1}	0.86
2	60	7.65×10^{-2}	0.87	1.82×10^{-1}	0.91
3	80	5.96×10^{-2}	0.91	1.40×10^{-1}	0.88
4	100	4.87×10^{-2}	0.93	1.15×10^{-1}	0.95
5	120	4.11×10^{-2}	0.93	9.67×10^{-2}	0.94
6	140	3.56×10^{-2}	0.94	8.37×10^{-2}	0.95
7	160	3.14×10^{-2}	—	7.37×10^{-2}	—

Table 6: Test A, error norms $e_{\infty,u}^{(N)}$ and $e_{\infty,w}^{(N)}$ using the limit scheme (20) for different meshes at time $T = 2$ with $\delta t = 2 \times 10^{-4}$

3.3.2 Test B: double shear layer

The initial data of the last test case are given by

$$u(x, y, 0) = \tanh\left(\frac{y - \frac{\pi}{2}}{\pi/15}\right) \mathbb{1}_{y \leq \pi} + \tanh\left(\frac{\frac{3\pi}{2} - y}{\pi/15}\right) \mathbb{1}_{y > \pi},$$

$$v(x, y, 0) = 0.05 \sin(x).$$

The exact solution is not known but we can compare with the results given in [15], based on computations with the ENO scheme on 64×64 and 128×128 grids. We perform a simulation

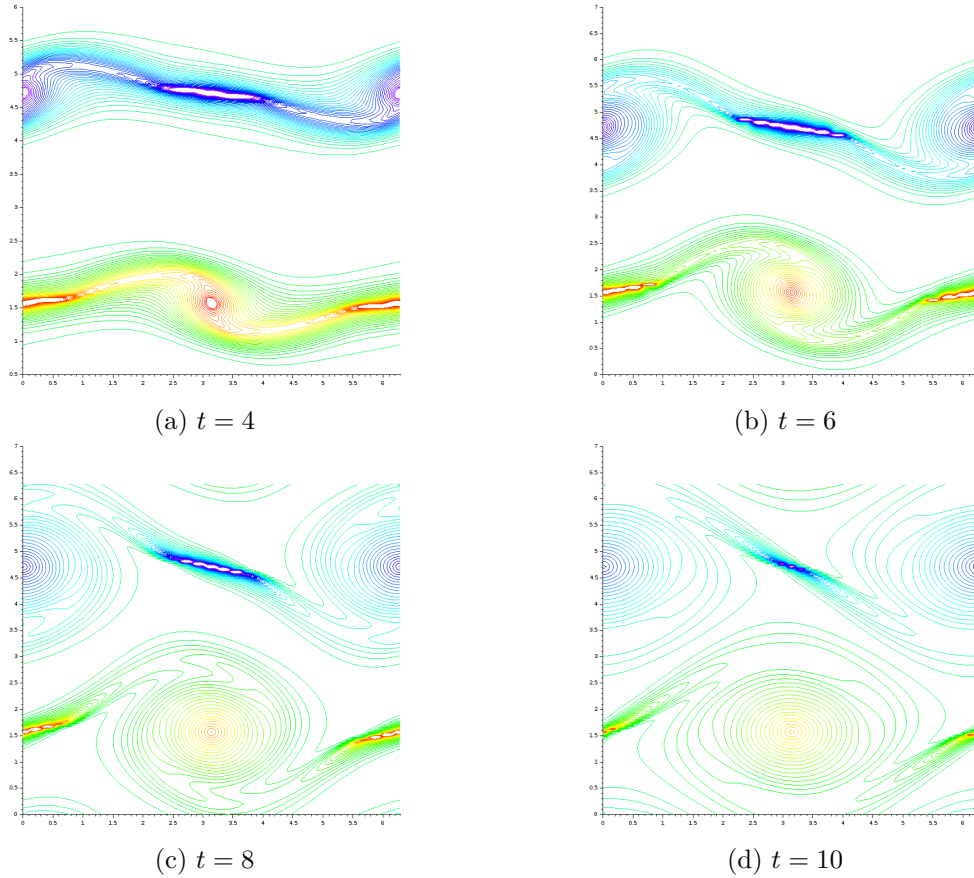


Figure 20: Test B (double shear layer), contour of the vorticity w at different times on a 128×128 grid with $\delta t = 10^{-3}$ using the limit scheme (20).

using the limit scheme (20) on a 128×128 grids. We display the vorticity in Figure 20 with 60 equally spaced contours from -4.9 to 4.9 at $t = 4$ (left up), $t = 6$ (right up), $t = 8$ (left bottom) and $t = 10$ (right bottom). These results are qualitatively very close to the ones obtained with the ENO scheme on the 64×64 grid in [15]. The ENO scheme used in [15] is fourth-order accurate (in the L^1 sense), while our scheme is only first order accurate. Nevertheless, the vortices developed by the solution with smaller and smaller scales are well reproduced.

References

- [1] T. Alazard. A minicourse on the low Mach number limit. *Discrete Contin. Dyn. Syst. Ser. S*, 1(3):365–404, 2008.
- [2] W. Barsukow, P. V. F. Edelmann, C. Klingenberg, F. Miczek, and F. K. Röpke. A numerical scheme for the compressible low-Mach number regime of ideal fluid dynamics. *J. Sci. Comput.*, 72(2):623–646, 2017.
- [3] F. Berthelin, T. Goudon, and S. Minjeaud. Kinetic schemes on staggered grids for barotropic Euler models: entropy-stability analysis. *Math. Comput.*, 84:2221–2262, 2015.

- [4] F. Berthelin, T. Goudon, and S. Minjeaud. Multifluid flows: a kinetic approach. *J. Sci. Comput.*, 66(2):792–824, 2016.
- [5] F. Bouchut, Y. Jobic, R. Natalini, R. Occelli, and V. Pavan. Second-order entropy satisfying BGK-FVS schemes for incompressible Navier-Stokes equations. *SMAI J. Comput. Math*, 2018. To appear.
- [6] F. Boyer. Analysis of the upwind finite volume method for general initial- and boundary-value transport problems. *IMA J. Numer. Anal.*, 32(4):1404–1439, 2012.
- [7] F. Coron and B. Perthame. Numerical passage from kinetic to fluid equations. *SIAM J. Numer. Anal.*, 28:26–42, 1991.
- [8] P. Degond and M. Tang. All speed scheme for the low Mach number limit of the isentropic Euler equations. *Comm. Comput. Phys.*, 10:1–31, 2011.
- [9] S. Dellacherie. Analysis of Godunov type schemes applied to the compressible Euler system at low Mach number. *J. Comput. Phys.*, 229(4):978–1016, 2010.
- [10] S. Dellacherie. *Etude et discrétisation de modèles cinétiques et de modèles fluides à bas nombre de Mach*. Habilitation à diriger les recherches, Université Pierre et Marie Curie - Paris VI, 2011.
- [11] S. Dellacherie, J. Jung, P. Omnes, and P.-A. Raviart. Construction of modified Godunov-type schemes accurate at any Mach number for the compressible Euler system. *Math. Models Methods Appl. Sci.*, 26(13):2525–2615, 2016.
- [12] S. Dellacherie, P. Omnes, and F. Rieper. The influence of cell geometry on the Godunov scheme applied to the linear wave equation. *J. Comput. Phys.*, 229:5315–5338, 2010.
- [13] S. M. Deshpande. Kinetic theory based new upwind methods for inviscid compressible flows. In *AIAA 24th Aerospace Science Meeting, Jan 6-9, 1986, Nevada, USA*, 1986. AIAA paper 86-0275.
- [14] G. Dimarco, R. Loubère, and M.-H. Vignal. Study of a new asymptotic preserving scheme for the Euler system in the low Mach number limit. *SIAM J. Sci. Comput.*, 39(5):A2099–A2128, 2017.
- [15] W. E and C.-W. Shu. A numerical resolution study of high order essentially non-oscillatory schemes applied to incompressible flow. *J. Comput. Phys.*, 110:39–46, 1993.
- [16] L. Gastaldo, R. Herbin, W. Kheriji, C. Lapuerta, and J.-C. Latché. Staggered discretizations, pressure correction schemes and all speed barotropic flows. In *Finite Volumes for Complex Applications VI, Problems and Perspectives, Prague, Czech Republic*, volume 4, pages 839–855, 2011.
- [17] H. Guillard and A. Murrone. On the behavior of upwind schemes in the low Mach number limit. II: Godunov type schemes. *Comput. Fluids*, 33:655–675, 2004.
- [18] H. Guillard and B. Nkonga. On the behaviour of upwind schemes in the low Mach number limit: a review. In *Handbook of numerical methods for hyperbolic problems*, volume 18 of *Handb. Numer. Anal.*, pages 203–231. Elsevier/North-Holland, Amsterdam, 2017.
- [19] H. Guillard and C. Viozat. On the behavior of upwind schemes in the low Mach number limit. *Comput. Fluids*, 28:63–86, 1999.

- [20] J. Haack, S. Jin, and J.-G. Liu. An all-speed asymptotic-preserving method for the isentropic Euler and Navier-Stokes equations. *Comm. Comput. Phys.*, 12:955–980, 2012.
- [21] F. H. Harlow and J. E. Welch. Numerical calculation of time-dependent viscous incompressible flow of fluid with free surface. *Phys. Fluids*, 8(12):2182–2189, 1965.
- [22] R. Herbin, W. Kheriji, and J.-C. Latché. Staggered schemes for all speed flows. *ESAIM:Proc*, 35:122–150, 2012. Actes du Congrès National de Mathématiques Appliquées et Industrielles.
- [23] R. Herbin, J.-C. Latché, and T. T. Nguyen. Explicit staggered schemes for the compressible Euler equations. In *Applied mathematics in Savoie—AMIS 2012: Multiphase flow in industrial and environmental engineering*, volume 40 of *ESAIM Proc.*, pages 83–102. EDP Sci., Les Ulis, 2013.
- [24] S. Jin. Efficient asymptotic-preserving (AP) schemes for some multiscale kinetic equations. *SIAM J. Sci. Comput.*, 21:441–454, 1999.
- [25] S. Jin. Asymptotic preserving (AP) schemes for multiscale kinetic and hyperbolic equations: a review. *Riv. Mat. Univ. Parma*, 3:177–216, 2012.
- [26] K. Kaiser, J. Schüte, R. Schöbel, and S. Noelle. A new stable splitting for the isentropic Euler equations. *J. Sci. Comput.*, 70:1390–1407, 2017.
- [27] S. Klainerman and A. Majda. Singular limits of quasilinear hyperbolic systems with large parameters and the incompressible limit of compressible fluids. *Comm. Pure Appl. Math.*, 34(4):481–524, 1981.
- [28] S. Klainerman and A. Majda. Compressible and incompressible fluids. *Comm. Pure Appl. Math.*, 35(5):629–651, 1982.
- [29] R. Klein. Semi-implicit extension of a Godunov-type scheme based on low Mach number asymptotics. I. One-dimensional flow. *J. Comput. Phys.*, 121(2):213–237, 1995.
- [30] R. LeVeque. *Numerical Methods for Conservation Laws*. Birkhauser, 1992.
- [31] J. Llobell. *Staggered discretization for conservation laws of gas dynamics*. PhD thesis, Université Côte d’Azur, Inria, CNRS, LJAD, 2018.
- [32] A. Majda. *Compressible fluid flow and systems of conservation laws in several space variables*. Springer Science +Business Media, LLC, 1984.
- [33] A. Majda and R. Pego. Stable viscosity matrices for systems of conservation laws. *J. Diff. Eqs.*, 56:229–262, 1985.
- [34] S. Noelle, G. Bispen, K. R. Arun, M. Lukáčová-Medvidóvá, and C.-D. Munz. A weakly asymptotic preserving low Mach number scheme for the Euler equations of gas dynamics. *SIAM J. Sci. Comput.*, 36(6):B989–B1024, 2014.
- [35] J. Schütz and S. Noelle. Flux splitting for stiff equations: A notion on stability. *J. Sci. Comput.*, pages 1–19, 2014.
- [36] E. Turkel. Preconditioned methods for solving the incompressible and low speed compressible equations. *J. Comput. Phys.*, 72:189–209, 1987.

- [37] S. Ukai. The incompressible limit and the initial layer of the compressible Euler equation. *J. Math. Kyoto Univ.*, 26(2):323–331, 1986.
- [38] H. Zakerzadeh and S. Noelle. A note on the stability of implicit-explicit flux-splittings for stiff systems of hyperbolic conservation laws. Technical report, Institut für Geometrie und Praktische Mathematik, RWTH Aachen, 2016. Report # 449.
- [39] C. Zaza. *Contribution à la résolution numérique d'écoulements à tout nombre de Mach et au couplage fluide-poreux en vue de la simulation d'écoulements diphasiques homogénéisés dans les composants nucléaires*. PhD thesis, Univ. Aix-Marseille, 2015.